The role of air–sea coupling in the simulation of the Madden–Julian oscillation in the Hadley Centre model

RMetS
Royal Meteorological Society

The role of air–sea coupling in the simulation of the Madden–Julian oscillation in the Hadley Centre model†

N. P. Klingaman* and S. J. Woolnough

National Centre for Atmospheric Science–Climate and Department of Meteorology, University of Reading, UK

*Correspondence to: N. P. Klingaman, Department of Meteorology, University of Reading, PO Box 243, Reading, Berkshire, RG6 6BB, UK. E-mail: n.p.klingaman@reading.ac.uk

The role of air–sea coupling in the simulation of the Madden–Julian oscillation (MJO) is explored using two configurations of the Hadley Centre atmospheric model (AGCM), GA3.0, which differ only in *F*, a parameter controlling convective entrainment and detrainment. Increasing *F* considerably improves deficient MJO-like variability in the Indian and Pacific Oceans, but variability in and propagation through the Maritime Continent remains weak.

By coupling GA3.0 in the tropical Indo-Pacific to a boundary-layer ocean model, K-profile parametrization (KPP), and employing climatological temperature corrections, well-resolved air–sea interactions are simulated with limited alterations to the mean state. At default *F*, when GA3.0 has a poor MJO, coupling produces a stronger MJO with some eastward propagation, although both aspects remain deficient. These results agree with previous sensitivity studies using AGCMs with poor variability. At higher *F*, coupling does not affect MJO amplitude but enhances propagation through the Maritime Continent, resulting in an MJO that resembles observations. A sensitivity experiment with coupling only in the Indian Ocean reverses these improvements, suggesting that coupling in the Maritime Continent and West Pacific is critical for propagation. We hypothesize that, for AGCMs with a poor MJO, coupling provides a 'crutch' to augment MJO-like activity artificially through high-frequency SST anomalies.

In related experiments, we employ the KPP framework to analyze the impact of air–sea interactions in the fully coupled GA3.0, which at default *F* shows a similar MJO to the uncoupled GA3.0. This is due to compensating effects: an improvement from coupling and a degradation from mean-state errors. Future studies on the role of coupling should separate these effects carefully.

Key Words: Madden–Julian oscillation; air–sea interactions; coupling; systematic errors; convection

Received 13 August 2013; Revised 22 October 2013; Accepted 5 November 2013; Published online in Wiley Online Library

1. Introduction

1.1. The Madden–Julian oscillation

The Madden–Julian oscillation (MJO: Madden and Julian, 1971) is the leading mode of subseasonal (30–60 day) tropical variability. The active MJO phase comprises a broad envelope of enhanced convection and precipitation, focused near the Equator, that often initiates in the Indian Ocean before propagating east through the Maritime Continent and into the Pacific. Suppressed convective conditions, slack westerly winds and strong insolation precede and follow the active phase. The MJO influences regional tropical weather and climate by modulating monsoon rainfall in Australia (Hendon and Liebmann, 1990; Wheeler *et al.*, 2009), Africa (Lavender and Matthews, 2009; Janicot *et al.*, 2010) and southeast Asia (Goswami *et al.*, 2006; Pai *et al.*, 2011), the latter due to a northwest–southeast tilted structure during boreal summer. When the active MJO reaches the West Pacific in boreal spring, the strong westerlies associated with the enhanced convection can trigger El Niño events via downwelling ocean Kelvin waves (Kessler *et al.*, 1995; Hendon and Wheeler, 2007). As the dynamical signal of the MJO circumnavigates the globe, it alters the probabilities of tropical cyclogenesis in the Indian, Pacific and Atlantic basins (Camargo *et al.*, 2009; Vitart, 2009). The circulation response to the MJO convective envelope extends into the extratropics, such that the MJO provides a source of predictability for, for example, the North Atlantic Oscillation and Atlantic blocking (Cassou, 2008; Vitart and Molteni, 2010).

†The copyright line for this article was changed on 27 February 2014 after original online publication.

1.2. Air–sea coupling and the simulation of the MJO

The MJO is strongly coupled to variability in air–sea fluxes and hence to variability in upper-ocean temperatures. Sea-surface temperature (SST) anomalies associated with subseasonal tropical convection have been observed during field campaigns (e.g. Anderson *et al.*, 1998; Bhat *et al.*, 2001) and in satellite observations (Woolnough *et al.*, 2000; Vecchi and Harrison, 2002; Klingaman *et al.*, 2008b). These SST anomalies, largely forced by the atmosphere (Jones *et al.*, 1998; Waliser *et al.*, 2004), exhibit a near-quadrature phase relationship with outgoing long-wave radiation (OLR): warm (cold) SSTs precede enhanced (suppressed) convection by 7–10 days (Fu *et al.*, 2003).

Over nearly 20 years, intercomparisons have repeatedly demonstrated that general circulation models (GCMs) struggle to capture the observed intensity, propagation speed, horizontal and vertical structure and teleconnections of tropical subseasonal variability (Slingo *et al.*, 1996; Lin *et al.*, 2006; Sperber and Annamalai, 2008; Kim *et al.*, 2009). Such intercomparisons have not identified a unifying characteristic among models that simulate the MJO well, nor a common failing among those that perform poorly. Many sensitivity studies have been conducted with one or several GCMs, focusing on horizontal resolution (Liess and Bengtsson, 2004; Jia *et al.*, 2008), vertical resolution (Inness *et al.*, 2001), the parametrization of deep convection (Zhu *et al.*, 2009; Benedict and Maloney, 2013), the accuracy of the tropical mean state (Inness *et al.*, 2003), the temporal resolution of prescribed SSTs (Kim *et al.*, 2008) and the presence and representation of air–sea coupling (Kemball-Cook *et al.*, 2002; Kim *et al.*, 2010). The results of these studies often conflict: similar changes applied to different GCMs produce opposite-signed impacts.

In particular, there is contention over the effect of coupling on the simulation of subseasonal convection. Sperber (2004) and Sperber *et al.* (2005) found that coupling improved the MJO in the National Center for Atmospheric Research Community Climate System Model (CCSM) and the Max Planck GCM (ECHAM4), respectively, although CCSM in particular still underestimated MJO amplitude considerably. More recently, Crueger *et al.* (2013) used many configurations of ECHAM6 to demonstrate that coupling enhanced MJO amplitude, though again all configurations displayed less subseasonal power than observed. In the Hadley Centre GCM (HadAM3), Inness and Slingo (2003) concluded that coupling improved MJO intensity and propagation; this was confirmed by Bernie *et al.* (2008) using a very high-resolution three-dimensional ocean model and by Klingaman *et al.* (2011) using a mixed-layer ocean for the boreal-summer MJO. A succession of hindcast studies found that coupling increased predictive skill for the MJO to a greater or lesser extent (Fu *et al.*, 2007; Woolnough *et al.*, 2007; Kim *et al.*, 2010). Yet Hendon (2000) found a degradation in MJO variability when the Geophysical Fluid Dynamics Laboratory (GFDL) GCM was coupled to a mixed-layer ocean. In contrast to studies showing an improved MJO with coupling, the GFDL atmospheric GCM (AGCM) overestimated rather than underestimated subseasonal variability. Likewise, Liess *et al.* (2004) found no improvement in the MJO with coupling in ECHAM4 when compared with an AGCM integration driven by the coupled-model SSTs. In aqua-planet simulations with a slab ocean, Grabowski (2006) demonstrated that interactive SSTs inhibited convective organization due to negative feedback between the SST anomalies and the strength of convection. Using a coupled linear inverse model, Newman *et al.* (2009) showed that air–sea interactions had little or no effect on simulated atmospheric subseasonal variability; coupled processes influenced the evolution of the atmosphere mainly on interannual time-scales.

Many of the sensitivity studies that concluded that coupling improved the MJO were performed with AGCMs that displayed weak subseasonal variability in organized, large-scale tropical variability. For example, HadAM3 had very little MJO-like activity when driven by monthly mean observed SSTs (Klingaman *et al.*, 2008a). In observations, however, the MJO is known to be a predominantly atmospheric mode of variability; AGCMs with parametrized (Benedict and Maloney, 2013) and super-parametrized or explicit convection (Khairoutdinov *et al.*, 2005) can capture the MJO. The sudden appearance of MJO-like variability in a coupled GCM (CGCM), where none exists the counterpart AGCM, raises the issue of whether coupled models are simulating the MJO by the correct (i.e. real-world) physical mechanisms. One hypothesis is that coupling introduces high-frequency SST variability that acts as a kind of 'crutch' for an AGCM, producing SST anomalies that can feed back on convection and encourage some degree of organization and propagation. Studies in which subseasonal tropical variability has been dramatically increased by prescribing daily or weekly observed SSTs in AGCMs, instead of monthly means, lend support to this hypothesis (Reicher and Roads, 2005; Kim *et al.*, 2008; Klingaman *et al.*, 2008a). The role of air–sea interactions in a CGCM in which the AGCM simulates adequate subseasonal variability requires further investigation.

The mean-state biases that inevitably result from air–sea coupling further complicate the analysis of the impact of coupling on the MJO. By comparing a standard coupled simulation of the Hadley Centre model (HadCM3) with one with heat-flux corrections, Inness *et al.* (2003) found that mean-state errors in HadCM3 prevented the propagation of the MJO into the Pacific. Several studies have attempted to quantify the impact of mean-state errors by prescribing climatological or otherwise temporally degraded CGCM SSTs in the AGCM (e.g. Fu and Wang, 2004), but this neglects the effect of mean-state errors on air–sea interactions (i.e. the role of coupling may depend on the mean state). Many investigations of the sensitivity of the simulated MJO to coupling have not estimated the impact of mean-state biases.

1.3. The purpose of the present study

The influence of air–sea interactions in the representation of the MJO in GCMs remains an open question, particularly because many AGCMs used to explore this sensitivity display poor subseasonal variability in tropical convection. The authors have recently improved the simulation of MJO-like variability in the Hadley Centre model, HadGEM3 (Walters *et al.*, 2011), by using hindcasts to explore the sensitivity of the simulated MJO to various physical parameters (Klingaman and Woolnough, 2013). Increasing by 50% the rates of entrainment (ϵ) and mixing detrainment (δ_m) for diagnosed deep and mid-level convection improved hindcast predictive skill, for this limited set of events, from 12 to 22 days. Klingaman and Woolnough (2013) briefly analyzed a 20 year simulation with the modified HadGEM3, finding that MJO activity approached observations, whereas a control simulation produced only half of the observed activity. MJO propagation also improved, but remained deficient relative to observations, particularly through the Maritime Continent.

This provides a rare opportunity to explore the effects of air–sea coupling on the representation of the MJO in highly similar configurations of a model that differ substantially in their levels of tropical subseasonal variability. We analyze these effects by conducting atmosphere-only and coupled simulations at default and higher ϵ and δ_m. We employ the coupling strategy of Klingaman *et al.* (2011), using many columns of a boundary-layer ocean model, with climatological heat corrections to maintain a similar mean state to the corresponding atmosphere-only integrations. This increases the likelihood that differences in MJO activity between coupled and uncoupled simulations are due to air–sea interactions rather than mean-state biases. We also demonstrate the effects on the MJO of mean-state SST errors from the fully coupled HadGEM3 (i.e. with a three-dimensional ocean

GCM) by conducting atmosphere-only and coupled simulations using the SSTs from the fully coupled model.

Section 2 describes the HadGEM3 configurations used in this study, the details of the coupling, the experiments performed and the datasets and analysis methods employed. Section 3 explores how the impact of air–sea interactions changes depending on the level of subseasonal variability in the AGCM. In section 4, we analyze the impact on MJO propagation of the K-profile parametrization (KPP) mean SSTs and coupling in the Maritime Continent and West Pacific, motivated by the results in section 3. Section 5 demonstrates a technique for separating the effect of coupling on the MJO in a fully coupled model into (i) the direct role of air–sea interactions and (ii) the role of mean-state errors. We discuss the results of this study in section 6 and summarize them in section 7.

2. Model, methods and data

2.1. HadGEM3 Global Atmosphere 3.0

All experiments use the HadGEM3 Global Atmosphere 3.0 (GA3.0: Arribas *et al.*, 2011; Walters *et al.*, 2011) AGCM. The horizontal resolution is 1.875° longitude × 1.25° latitude with 85 points in the vertical −50 of which are in the tropical troposphere (18 km) −and a rigid lid at 85 km. HadGEM3 is under development, but GA3.0 is a fixed scientific configuration of the model. Klingaman and Woolnough (2013) used a slightly older configuration, GA2.0, to explore the role of increased entrainment and detrainment rates on the simulated MJO. There are only slight differences in MJO activity between GA2.0 and GA3.0; the effect of increasing ϵ and δ_{m} is also similar (see section 3.1). Walters *et al.* (2011) describes the differences between GA2.0 and GA3.0.

Of particular consequence to this study are the formulations of ϵ and δ_{m} in the modified Gregory and Rowntree (1990) convection scheme in GA3.0. Entrainment for diagnosed deep and mid-level convection is parametrized at each vertical gridpoint (z) as

$$\epsilon(z) = 4.5F\frac{p(z)\rho(z)g(z)}{p_*^2}, \tag{1}$$

where F is a scaling factor, p and ρ are pressure and density, g is gravity and p_* is surface pressure. We increase ϵ by increasing F, which also increases δ_{m} for deep convection:

$$\delta_{\mathrm{m}}(z) = 1.5[1 - R(z)]\epsilon(z), \tag{2}$$

where R is relative humidity. The parcel is forced to detrain completely at the level of neutral buoyancy (i.e. there is no 'overshooting'). Further details can be found in Stratton *et al.* (2009), Derbyshire *et al.* (2011) and Walters *et al.* (2011).

2.2. Coupling to the KPP model

We couple GA3.0 to many columns of the KPP boundary-layer ocean model (Large *et al.*, 1994) via the Ocean–Atmosphere–Sea Ice–Soil (OASIS: Valcke *et al.*, 2003) coupler, version 3. We refer to this model as GA3.0-KPP. The coupling strategy is identical to that for HadKPP in Klingaman *et al.* (2011), but with updated versions of the AGCM and OASIS.

As KPP simulates only vertical mixing, depth-varying temperature corrections are used to constrain the monthly mean ocean temperature profile towards a reference climatology. This climatology is taken from either observations or a fully coupled version of HadGEM3 (see section 2.3). The corrections are computed as in Klingaman *et al.* (2011): for each GA3.0-KPP integration, the surface fluxes from each of the first ten years of the corresponding GA3.0 integration are used to drive a one-year KPP integration. At the end of each month, the KPP integration is paused; the profile of corrections required to remove the monthly mean temperature bias is computed; the profile is then imposed in a second integration for that month, before continuing to the next month. The climatological, monthly mean corrections are computed from the ten years of KPP integrations and imposed in GA3.0-KPP. In the forced KPP and GA3.0-KPP simulations, salinity is relaxed to the climatological, monthly mean profile with a 90-day timescale. This damps seasonal-time-scale salinity variability but, as our focus is subseasonal variability, this damping is not expected to affect our results.

By constraining ocean temperature and salinity, GA3.0-KPP produces small SST biases and hence a similar mean state to the corresponding GA3.0 simulations (see section 3.2). This limits the possibility that differences in MJO behaviour between GA3.0 and GA3.0-KPP simulations are due to changes in the mean state. Section 4.1 tests the role of the climatological GA3.0-KPP SSTs in MJO propagation.

2.3. Experiments

All experiments are labelled by [experiment type]-[entrainment]-[SST boundary condition]. Experiment type is either 'A' (atmosphere-only) or 'K' (KPP-coupled); for the latter, a subscript denotes the coupling region as either 'WP' (Warm Pool: 30°N–30°S, 20°–200°E) or 'IO' (Indian Ocean: 30°N–30°S, 20°–100°E). Table 1 summarizes the experiments, which are all 20 years long.

A set of four experiments are conducted using GA3.0 and GA3.0-KPP with default and higher F: A-CTL-OBS, $\mathrm{K_{WP}}$-CTL-OBS, A-ENT-OBS and $\mathrm{K_{WP}}$-ENT-OBS. In A-CTL-OBS and A-ENT-OBS, SSTs and sea ice are prescribed from a monthly mean climatology (1980–2009) of the Met Office ocean analysis (Smith and Murphy, 2007). In $\mathrm{K_{WP}}$-CTL-OBS and $\mathrm{K_{WP}}$-ENT-OBS, KPP is constrained to the temperature and salinity profiles from that climatology within the coupled region (Table 1). Outside that region, the Smith and Murphy (2007) climatological SSTs and sea ice are prescribed; a five-point linear blending is applied at the boundaries to reduce SST gradients.

Two sensitivity tests are performed to understand the results of $\mathrm{K_{WP}}$-ENT-OBS: a GA3.0 integration with prescribed $\mathrm{K_{WP}}$-ENT-OBS climatological SSTs (A-ENT-$\mathrm{K_{WP}}$) and a GA3.0-KPP integration with the eastern coupling boundary at the western edge of the Maritime Continent ($\mathrm{K_{IO}}$-ENT-OBS). The role of coupled-model mean-state biases is investigated with the climatology of a 30-year integration of GA3.0 coupled to the Nucleus for European Modelling of the Ocean (NEMO) model (GA3.0-NEMO), the standard ocean model for HadGEM3. The A-CTL-NEMO and $\mathrm{K_{WP}}$-CTL-NEMO experiments are as in A-CTL-OBS and $\mathrm{K_{WP}}$-CTL-OBS, but replace the Met Office ocean climatology with the NEMO climatology; section 5.1 contains further information on these experiments and the motivation behind them.

2.4. Methods and data

In simulations and observations, MJO activity is assessed through the Real-time Multivariate MJO (RMM) indices of Wheeler and Hendon (2004). RMM indices are computed from model data using the method outlined there, except that no regression on ENSO is removed; there is no ENSO in any integration due to the use of climatological SSTs. We project model anomalies on to the observed RMM empirical orthogonal functions (EOFs). The observed RMM indices for 1975–2011 are taken from Matt Wheeler's website (http://www.cawcr.gov.au/staff/mwheeler/maproom/RMM).

As in Klingaman and Woolnough (2013), we diagnose MJO 'activity' as the fraction of days in which the RMM amplitude is ≥ 1 ('strong MJO'), for all RMM phases and for each phase separately, as shown in Figure 1. That study demonstrated that this measure was strongly linked to other diagnostics of tropical

Table 1. A summary of the experiments analyzed in this study, including the label used in the text, the value of the *F* parameter controlling entrainment and mixing detrainment, the domain in which the atmosphere is coupled to KPP, if any, and the SST boundary condition used outside the coupling region. All experiments are 20 years long.

Label	Value of *F*	Coupling	SST boundary condition
A-CTL-OBS	0.90	Atmosphere-only	Climatological observed
A-ENT-OBS	1.35	Atmosphere-only	Climatological observed
K_{WP}-CTL-OBS	0.90	KPP 30°S–30°N, 20°–200°E	Climatological observed
K_{WP}-ENT-OBS	1.35	KPP 30°S–30°N, 20°–200°E	Climatological observed
A-ENT-K_{WP}	1.35	Atmosphere-only	Climatological K-ENT-OBS
K_{IO}-ENT-OBS	1.35	KPP 30°S–30°N, 20°–100°E	Climatological observed
A-CTL-NEMO	0.90	Atmosphere-only	Climatological GA3.0-NEMO
K_{WP}-CTL-NEMO	0.90	KPP 30°S–30°N, 20°–200°E	Climatological GA3.0-NEMO

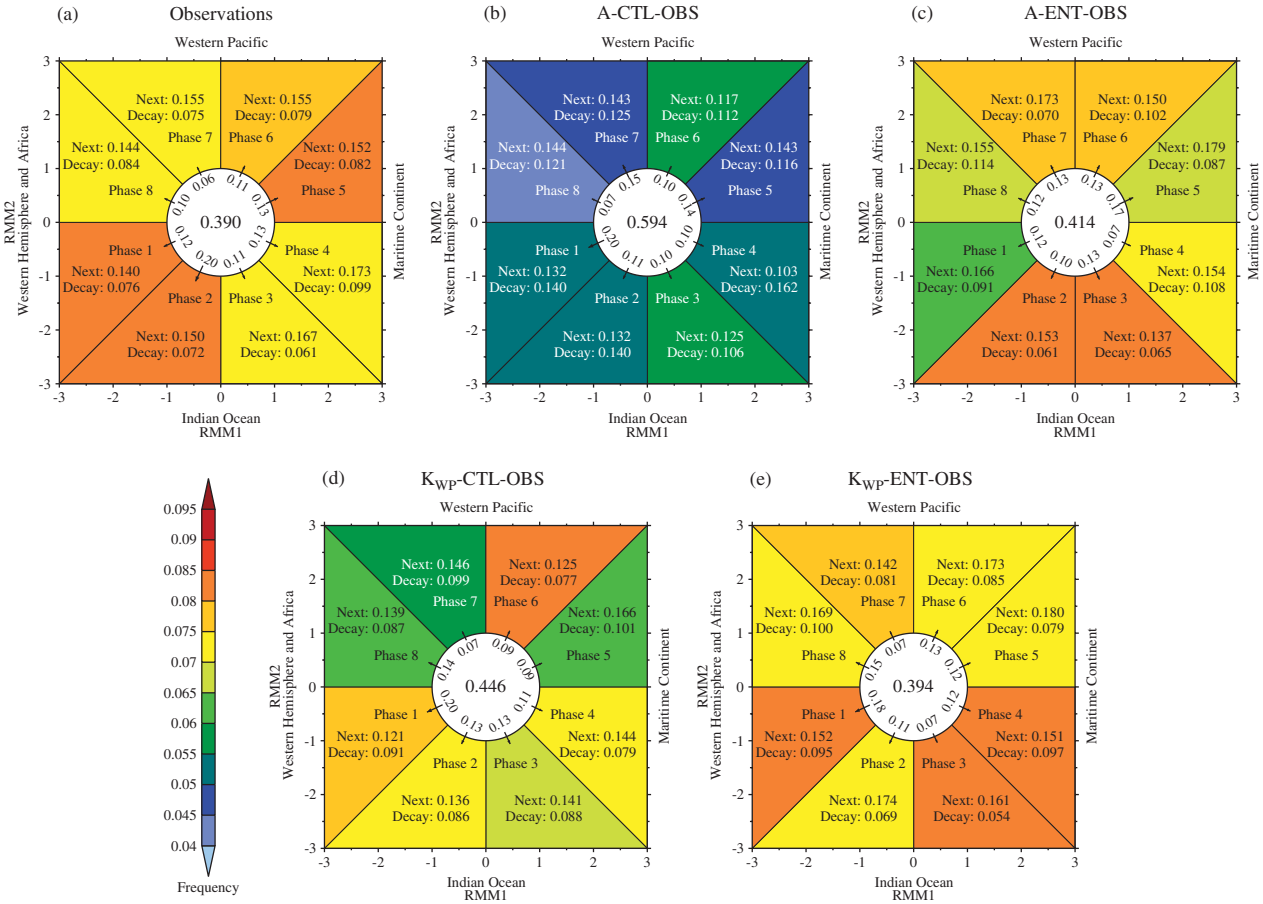

Figure 1. For (a) observations (1975–2012), (b) A-CTL-OBS, (c) A-ENT-OBS, (d) K_{WP}-CTL-OBS and (e) K_{WP}-ENT-OBS, the coloured wedges show the daily frequency of strong activity (amplitude ≥ 1) in each phase, relative to all days in the integration, using the colour scale to the left of (d). For each phase, the decimal fractions are probabilities that, on the day following strong activity in that phase, the MJO transitions to the next (anticlockwise) phase ('Next') or moves into the unit circle ('Decay', i.e. an amplitude less than one). The frequency of weak MJO activity is given inside the unit circle. The values next to the arrows crossing the unit circle show the relative probabilities of MJO genesis in each phase.

subseasonal variability, such as wavenumber–frequency power spectra, and was a useful 'one-look' measure of MJO activity in a GCM. Phase composites are constructed by taking the average of a quantity over all days with amplitude ≥ 1 in that phase. These composites are computed using anomalies from a daily climatology. We also remove the mean of the previous 120 days before each day in each phase composite to isolate intra-seasonal signals, as in Wheeler and Hendon (2004).

To assess zonal propagation, we compute lag regressions of latitude-averaged (10°N–10°S), 20–100 day bandpass-filtered OLR using base points in the central Indian Ocean (70°E) and the western (100°E) and eastern (130°E) edges of the Maritime Continent. The latter two points are selected to focus on propagation through the Maritime Continent. This diagnostic is recommended by the CLIVAR MJO Task Force (Kim *et al.*, 2009).

OLR data are taken from the National Oceanic and Atmospheric Administration (NOAA) Advanced Very High Resolution Radiometer (AVHRR) dataset for 1979–2012 on a 2.5°×2.5° horizontal grid. Rainfall data come from the Tropical Rainfall Measuring Mission (TRMM: Kummerow *et al.*, 1998) 3B42 product, version 6, for 1998–2012 on a 0.25°×0.25° grid. SST data are obtained from the blended TRMM Microwave Imager (TMI: Wentz, 2000) and Advanced Microwave Scanning Radiometer (AMSRE) product from Remote Sensing Systems for 1998–2012, on the TRMM grid. Daily mean, pressure-level specific-humidity data are taken from the European Centre for Medium-range Weather Forecasts Interim reanalysis (ERA-Interim: Uppala *et al.*, 2005) for 1989–2008. Rainfall, SSTs and specific humidity are interpolated to the GA3.0 grid, using an area-weighted method.

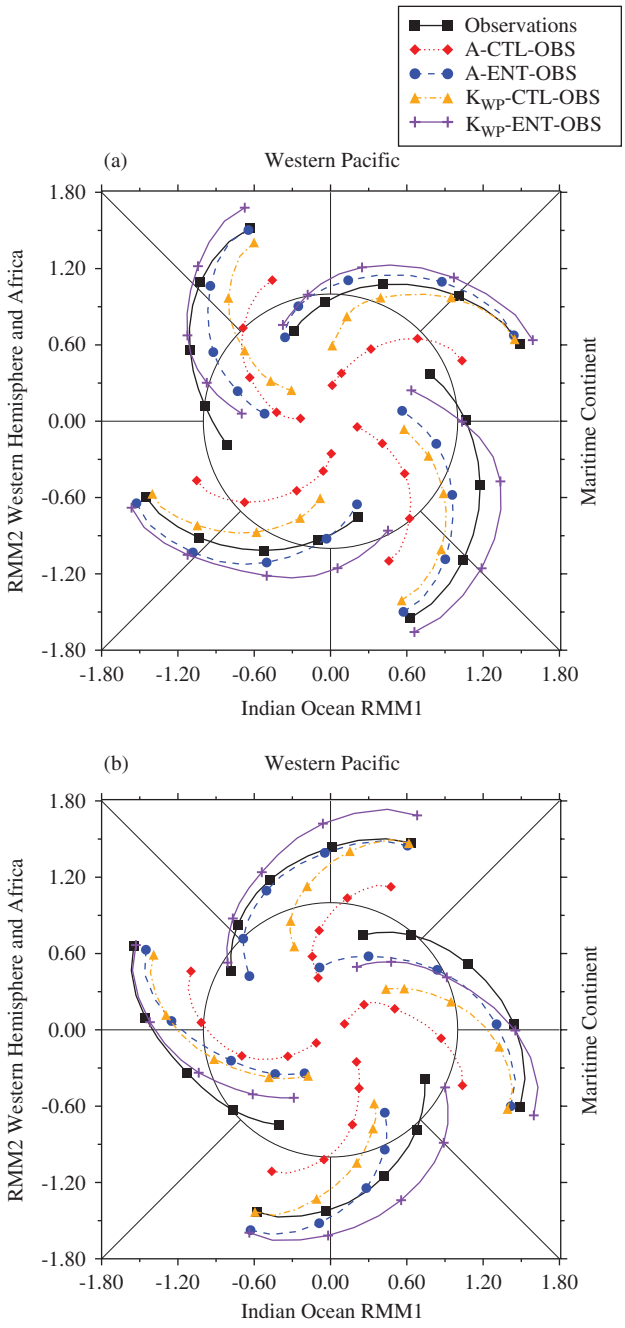

Figure 2. Lag composites of RMM indices for strong MJO activity in each phase, with symbols spaced every 3 days (12 days in total), for observations (black), A-CTL-OBS (red), A-ENT-OBS (blue), K_{WP}-CTL-OBS (orange) and K_{WP}-ENT-OBS (purple). Composites of odd-numbered phases are shown in (a); even-numbered phases are shown in (b).

3. The roles of air–sea coupling at standard and higher entrainment

3.1. *Atmosphere-only simulations*

In observations, 61% of days have a strong MJO in any phase (Figure 1(a)). By contrast, 41% of days in A-CTL-OBS have a strong MJO (Figure 1(b)). This percentage is higher than that (34%) for the 20 year GA2.0 control integration in Klingaman and Woolnough (2013), suggesting the MJO is slightly stronger in GA3.0. Still, A-CTL-OBS produces only 65% of the observed MJO activity by this measure. Lag composites of strong MJO activity show that A-CTL-OBS is often unable to maintain a strong MJO beyond three days (Figure 2), as the composites quickly decay into the unit circle with little propagation. In observations, the composites remain outside the unit circle for 8–10 days. In A-CTL-OBS, the probability of a strong MJO event 'decaying' into the unit circle on the next day is 50–100% greater than observed in all phases (compare Figure 1(a) and (b)). The probability of decay was separated into 'death' –in which the RMM index remains <1 for 10 days or more –and 'illness' –10 days or less (not shown); in observations and all simulations, illness (death) accounted for about two-thirds (one-third) of decay. Illness indicates an intermittent MJO, while death can be used to separate events.

Phase composites of TRMM rainfall anomalies show the canonical eastward movement of heavy rainfall from the Indian Ocean (Figure 3(a)) to the Maritime Continent (Figure 3(b)) and the West Pacific (Figure 3(c)), with negative anomalies to the west and east. (For brevity, we focus on RMM phases 2, 4 and 6 throughout the study.) A-CTL-OBS displays much less spatial coherence and weaker anomalies in all phases (Figure 3(d)–(f)), with the strongest (weakest) anomalies off (on) the Equator, whereas the observations typically have maxima on the Equator. Weak equatorial variability in convection is a known bias in Hadley Centre models (Yang *et al.*, 2009). This is particularly evident in phase 2: there is no suppressed convection in the West Pacific and a meridional split in the active phase across the Indian Ocean.

To examine eastward propagation, we compute lag regressions of latitude-averaged (10°S–10°N), 20–100 day bandpass-filtered OLR against base points at 70°E, 100°E and 130°E (section 2.4). The observations show clear eastward propagation of active and suppressed phases (Figure 4(a)–(c)). In A-CTL-OBS, subseasonal OLR variability is either stationary or propagates west (Figure 4(d)–(f)).

As in Klingaman and Woolnough (2013) for GA2.0, using $1.5F$ (1) raises MJO activity in A-ENT-OBS (58.6%; Figure 1(c)) to near-observed levels (61.1%; Figure 1(a)). The distribution of activity around the phase space is skewed towards the Indian Ocean and West Pacific phases (2, 3, 6 and 7), with relatively less activity near the Maritime Continent and in the Western Hemisphere (4, 5, 8 and 1). A-ENT-OBS favours variability in Wheeler and Hendon (2004) EOF1 –the anticorrelation between the Indian Ocean and West Pacific –over EOF2, which describes intraseasonal variability over the Maritime Continent.

Lag composites in RMM space demonstrate longer lifetimes for strong MJO events in most phases in A-ENT-OBS over A-CTL-OBS (Figure 2). Events in the Indian Ocean, in particular, propagate further through phase space before decaying into the unit circle. The mean RMM amplitude in each phase (blue circles) increases substantially in A-ENT-OBS. The origin in phase space, equivalent to no projection on to either Wheeler and Hendon (2004) EOF, remains a strong attractor even in A-ENT-OBS. RMM phase composites of rainfall anomalies show an increase in magnitude, with increased equatorial rainfall variability compared to A-CTL-OBS (Figure 3(g)–(i)). The anomalies are more spatially coherent, particularly in the Indian Ocean in phase 2 (Figure 3(g)). Substantial biases remain, including an erroneous extension of positive (negative) rainfall anomalies in phase 2 (phase 6) from the Indian Ocean into the West Pacific, where the observations show negative (positive) anomalies. While the observations show enhanced rainfall extending northwest from the Maritime Continent to India in phase 4 (Figure 3(b)), no such extension exists in A-ENT-OBS (Figure 3(h)).

Although MJO propagation improves in A-ENT-OBS (Figure 4(g)–(i)) relative to A-CTL-OBS, it remains deficient. In particular, active (suppressed) convection in the Indian Ocean (Figure 4(g)) fails to move coherently across the Maritime Continent. Similarly, the active phases over the Maritime Continent (Figure 4(h)) are not strongly connected to convection propagating from the Indian Ocean or to the West Pacific, as in observations (Figure 4(b)). Combined with the too-strong (too-weak) variability in RMM1 (RMM2), this suggests that instead of a coherent, propagating MJO, A-ENT-OBS produces a standing oscillation between the Indian Ocean and West Pacific that projects on to the Wheeler and Hendon (2004) EOFs.

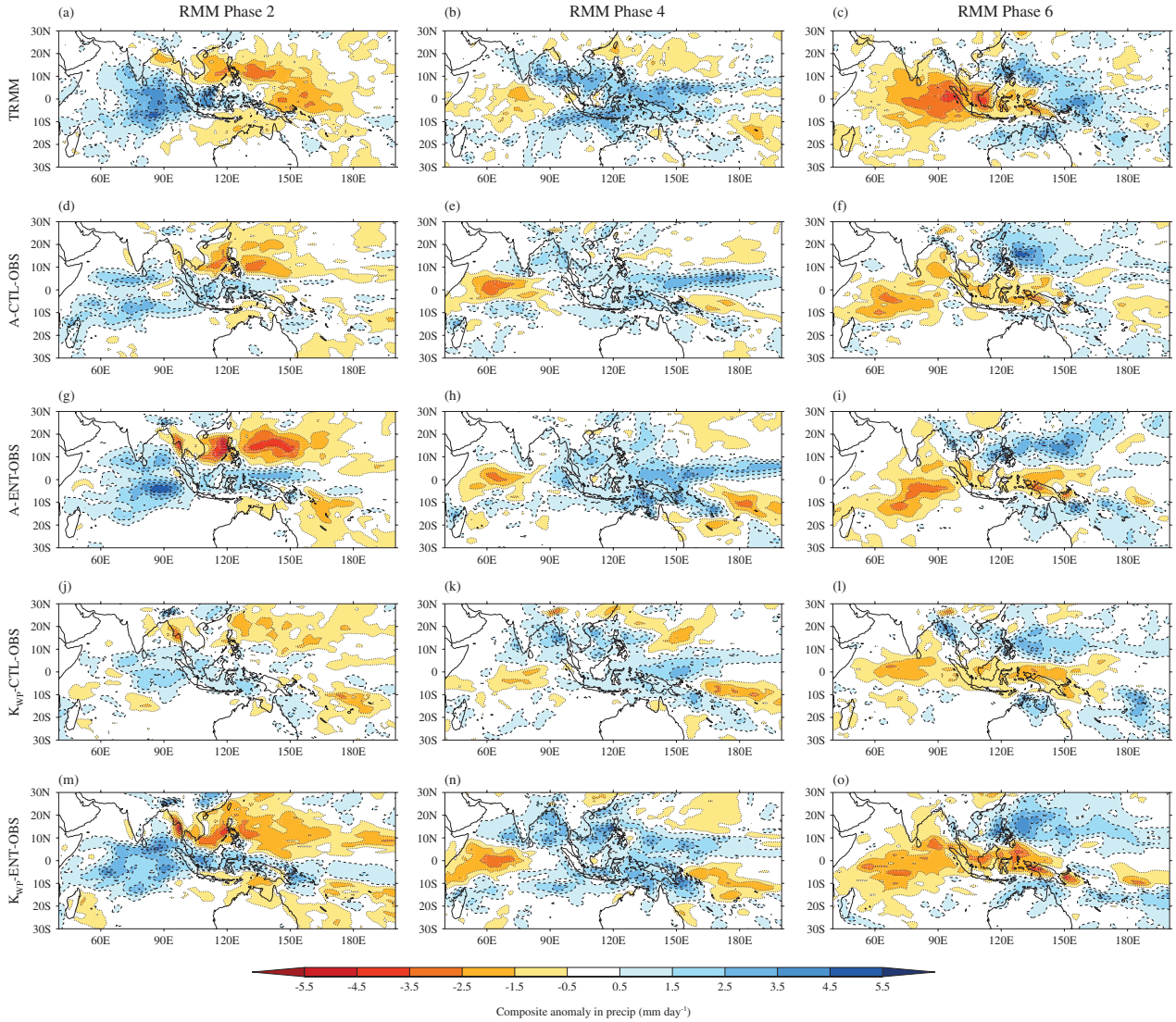

Figure 3. Phase composites of daily mean precipitation anomalies (mm day^{-1}) taken from the daily climatology of each dataset. Positive (negative) contours are dashed (dotted).

3.2. *Air–sea coupling at standard entrainment*

Comparing K_{WP}-CTL-OBS and A-CTL-OBS reveals the impact of air–sea coupling at default F, when GA3.0 has a poor MJO. Coupling to KPP produces changes in tropical rainfall and SST that are generally less than 1 mm day^{-1} and 0.2 K, respectively, but locally up to 2 mm day^{-1} and 0.5 K (Figure 5). The warm SSTs and increased rainfall around the Maritime Continent may influence MJO propagation; we test the effects of the mean SST change in section 4.1.

K_{WP}-CTL-OBS (Figure 1(d)) has more frequent MJO activity (55% of days) than A-CTL-OBS (Figure 1(b)). This is somewhat lower than observed (61%) and A-ENT-OBS (59%), but indicates that coupling to KPP improves intraseasonal variability at default F. The lifetimes of K_{WP}-CTL-OBS composite MJO events are longer than in A-CTL-OBS in all phases, particularly those in the Indian Ocean and Maritime Continent (Figure 2). Amplitude and propagation are weaker than in A-ENT-OBS, however. Klingaman *et al.* (2011) found that coupling to KPP made similar improvements to boreal-summer MJO amplitude and lifetimes in HadAM3, which also demonstrated poor subseasonal variability in atmosphere-only integrations.

Phase composites of K_{WP}-CTL-OBS rainfall anomalies (Figure 3(j)–(l)) are similar to A-ENT-OBS (Figure 3(g)–(i)), with somewhat smaller magnitudes, and thus show similar improvements against A-CTL-OBS (Figure 3(d)–(f)). Indian Ocean equatorial precipitation anomalies still extend too far through the Maritime Continent in phases 2 and 6 (Figure 3(j) and (l)), but the extension is less than in A-ENT-OBS or A-CTL-OBS. The observed northwest tilt of enhanced convection from the Maritime Continent to India in phase 4 (Figure 3(b)) is more apparent in K_{WP}-CTL-OBS (Figure 3(k)) than in A-ENT-OBS (Figure 3(h)). This is likely due to a more frequent occurrence of phase 4 in K_{WP}-CTL-OBS in boreal summer (not shown), when the MJO rainband tilts northwest. Lag regressions of 20–100 day OLR (Figure 4(j)–(l)) demonstrate improvements against A-CTL-OBS (Figure 4(d)–(f)). Propagation is similar to A-ENT-OBS (Figure 4(g)–(i)), with some eastward movement from the Indian Ocean but little propagation through the Maritime Continent. In GA3.0, air–sea coupling somewhat improves amplitude and propagation at default F, but both remain deficient.

Air–sea coupling has been found to improve the phase relationship between anomalies in SST and convection (Woolnough *et al.*, 2001; Fu and Wang, 2004; Rajendran and Kitoh, 2006). A-CTL-OBS and A-ENT-OBS have coincident, positive correlations between OLR and SST anomalies, while K_{WP}-CTL-OBS and K_{WP}-ENT-OBS show a near-quadrature relationship with warm (cold) SSTs leading negative (positive) OLR anomalies by seven days (not shown), somewhat shorter than the observed lead of ten days (Vecchi and Harrison, 2002). To examine the spatial structure of MJO SST anomalies, phase composites were constructed as for rainfall (Figure 6). For TMI/AMSRE SSTs, much of the Indian Ocean and Maritime Continent is

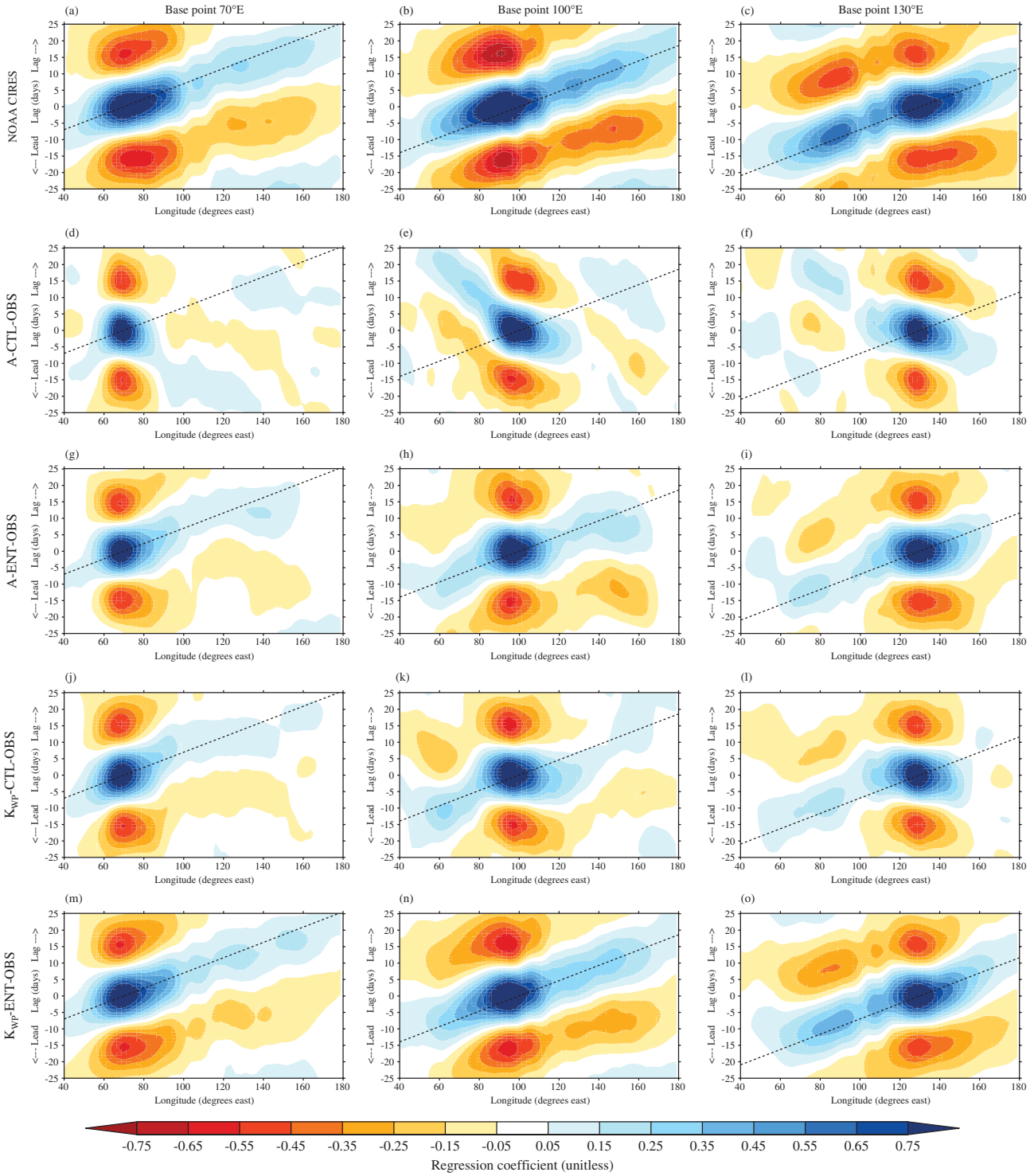

Figure 4. Lag regressions of latitude-averaged (10°S–10°N), 20–100 day bandpass-filtered OLR against base points at (a, d, g, j, m) 70°E, (b, e, h, k, n) 100°E and (c, f, i, l, o) 130°E. Positive (negative) days are lags (leads). The dashed lines are 4.35° day^{-1}, approximately the observed propagation speed.

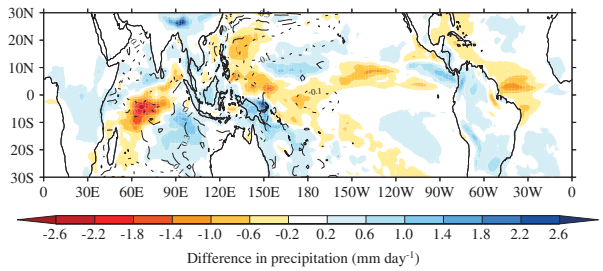

Figure 5. For K_{WP}-CTL-OBS minus A-CTL-OBS, annual mean differences in (shading) precipitation (mm day^{-1}) and (contours) SST [interval 0.2 K from ±0.1 K; positive (negative) dashed (dotted)] are shown. SST differences are zero outside the coupling region (30°S–30°N, 20°–200°E), since K_{WP}-CTL-OBS and A-CTL-OBS use the same prescribed SSTs.

anomalously warm during phase 2 (Figure 6(a)), except for near the Equator where the strongest TRMM rainfall anomalies occur (Figure 3(a)). The warm anomalies are weaker in K_{WP}-CTL-OBS (Figure 6(d)), consistent with the smaller rainfall anomalies (Figure 3(j)) and suggesting weaker-than-observed surface forcing. Phases 4 and 6 (Figure 6(e) and (f)) also show much weaker anomalies than observed (Figure 6(b) and (c)).

When GA3.0 has poor subseasonal variability (i.e. A-CTL-OBS), coupling improves MJO amplitude, propagation and spatial structure. None of these characteristics reaches observed levels: MJO activity is too low, propagation is limited to the Indian Ocean and the structure is still zonally elongated on the Equator. Air–sea feedback may act to amplify and organize the MJO in AGCMs with weak subseasonal variability in tropical convection.

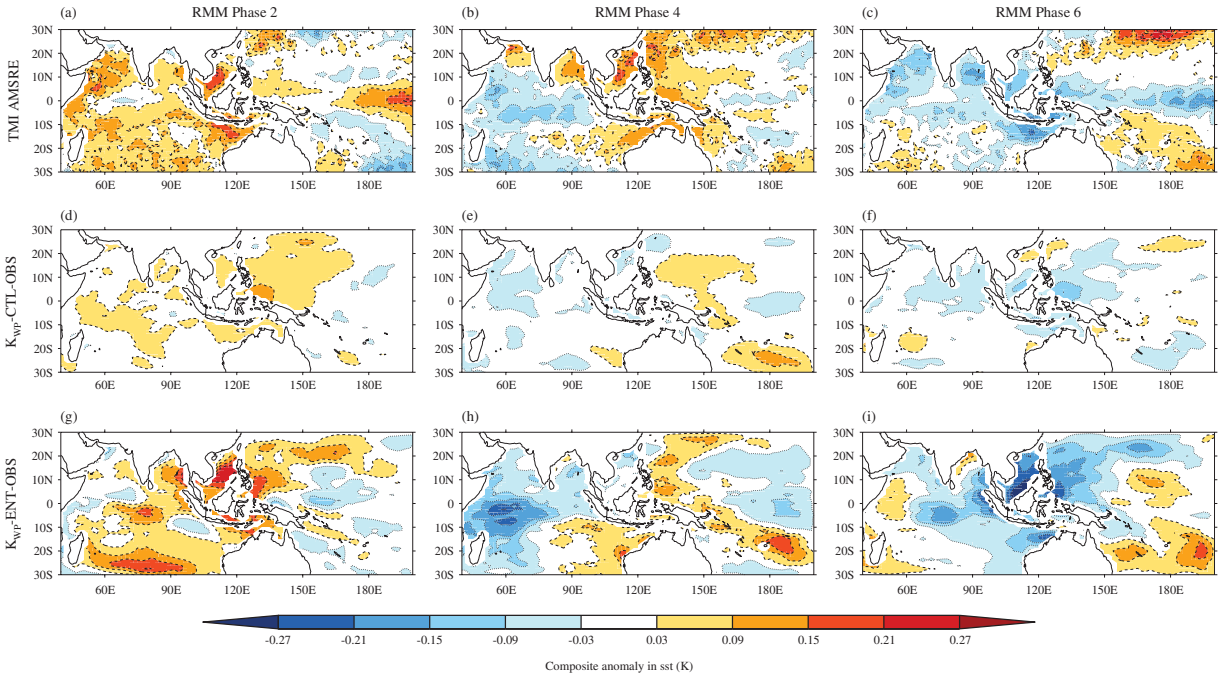

Figure 6. As in Figure 3, but for phase composites of daily mean SST anomalies from (a)–(c) TMI/AMSRE, (d)–(f) K_{WP}-CTL-OBS and (g)–(i) K_{WP}-ENT-OBS. Positive (negative) contours are dotted (dashed).

3.3. *Air–sea coupling at higher entrainment*

Comparing K_{WP}-ENT-OBS and A-ENT-OBS demonstrates the role of coupling at 1.5*F*, when GA3.0 has improved tropical subseasonal variability. The differences in mean precipitation and SST between K_{WP}-ENT-OBS and A-ENT-OBS (not shown) are similar to those in Figure 5.

K_{WP}-ENT-OBS has similar total MJO activity (60.6%: Figure 1(e)) to A-ENT-OBS (58.6%: Figure 1(c)). This contrasts with section 3.2, in which coupling increased MJO activity at default *F*. The distribution of activity in K_{WP}-ENT-OBS is more equitable than in A-ENT-OBS: activity increases in the Maritime Continent (phases 4 and 5) and the Western Hemisphere (phases 8 and 1) and decreases in the Indian Ocean (2 and 3) and West Pacific (6 and 7). This improves the biases in A-ENT-OBS (section 3.1), bringing the frequency of each phase closer to observations (Figure 1(a)). K_{WP}-ENT-OBS has longer MJO lifetimes in nearly all phases than A-ENT-OBS (Figure 2). In particular, the phase 2 composite in K_{WP}-ENT-OBS propagates much further outside the unit circle, reaching the boundary with phase 4, as in observations.

Improved propagation across the Maritime Continent is also apparent from regressions of 20–100 day filtered OLR (Figure 4(m)–(o)). Using a base point in the Indian Ocean (70°E), K_{WP}-ENT-OBS displays coherent eastward movement through the Maritime Continent with approximately the observed phase speed (Figure 4(m)). OLR anomalies over the Maritime Continent lag those over the Indian Ocean and lead those in the West Pacific (Figure 4(n)). Regression coefficients are slightly smaller than in observations, indicating weaker coherent intraseasonal OLR variability, but propagation improves over A-ENT-OBS (Figure 4(g)–(i)).

Coupling also improves the spatial coherence of MJO-related precipitation. Phase 2 anomalies in K_{WP}-ENT-OBS (Figure 3(m)) are more strongly focused in the Indian Ocean than in A-ENT-OBS (Figure 3(g)). The zonally elongated anomalies in A-ENT-OBS are less apparent in K_{WP}-ENT-OBS, although weak positive anomalies still exist east of the Maritime Continent. Similar improvements can be seen in phases 4 (compare Figure 3(n) and(h)) and 6 (compare Figure 3(o) and (i)). In phase 4, the spatial pattern in K_{WP}-ENT-OBS is closer to TRMM (Figure 3(b)), with a clear westward tilt with latitude away from the Equator.

K_{WP}-ENT-OBS displays stronger and more coherent rainfall anomalies than K_{WP}-CTL-OBS (Figure 3(j)–(l)). Associated with these are more intense SST anomalies (Figure 6(g)–(i)), particularly near the Maritime Continent, where MJO propagation shows the greatest improvement. The magnitude of the K_{WP}-ENT-OBS anomalies agrees with TMI/AMSRE (Figure 3(a)–(c)), with a similar spatial pattern. K_{WP}-ENT-OBS produces SST anomalies in the western Indian Ocean of the opposite sign to TMI/AMSRE, which may be due to the too-short phase lag between convection and SST (see section 3.2). When GA3.0 has a reasonable level of MJO activity, then, air–sea coupling does not further increase MJO amplitude or frequency of occurrence –as when the model has poor subseasonal variability –but instead improves the organization and propagation of convection.

To analyze the effect of coupling on the vertical structure of the MJO in the 1.5*F* simulations, we use phase composites of latitude-averaged (15°S–15°N) specific humidity anomalies from the model and ERA-Interim (Figure 7). Although reanalysis humidity is influenced by the convective parametrization of the model used to produce the reanalysis, large-scale moisture variations should be reasonably well-constrained by observations. In phase 2, ERA-Interim shows deep moisture anomalies in the eastern Indian Ocean near 90°E and a westward tilt with height; there are shallow positive anomalies across the Maritime Continent, with mid- and upper-level dry anomalies extending to the West Pacific (Figure 7(a)). A-ENT-OBS has weaker anomalies, little zonal tilt with height and a pronounced peak in moisture anomalies near the freezing level (Figure 7(d)). The positive anomalies over the Maritime Continent are too deep, consistent with the zonal elongation of equatorial rainfall anomalies (Figure 3(g)), suggesting convection still deepens too quickly in this region even at 1.5*F*. By contrast, K_{WP}-ENT-OBS (Figure 7(g)) shows moisture anomalies that are more concentrated in the Indian Ocean, with the strongest anomalies extending throughout the lower and mid troposphere, rather than the narrow, mid-level peak in A-ENT-OBS. K_{WP}-ENT-OBS also has a stronger westward tilt with height, although the positive anomalies over the Maritime Continent are still deeper than in ERA-Interim. The mid- and upper-level dry anomalies in K_{WP}-ENT-OBS suggest that air–sea coupling improves the persistence of suppressed conditions east of the active phase. The cold SST anomalies in the West Pacific in phase 2 in K_{WP}-ENT-OBS (Figure 6(g)), presumably from the

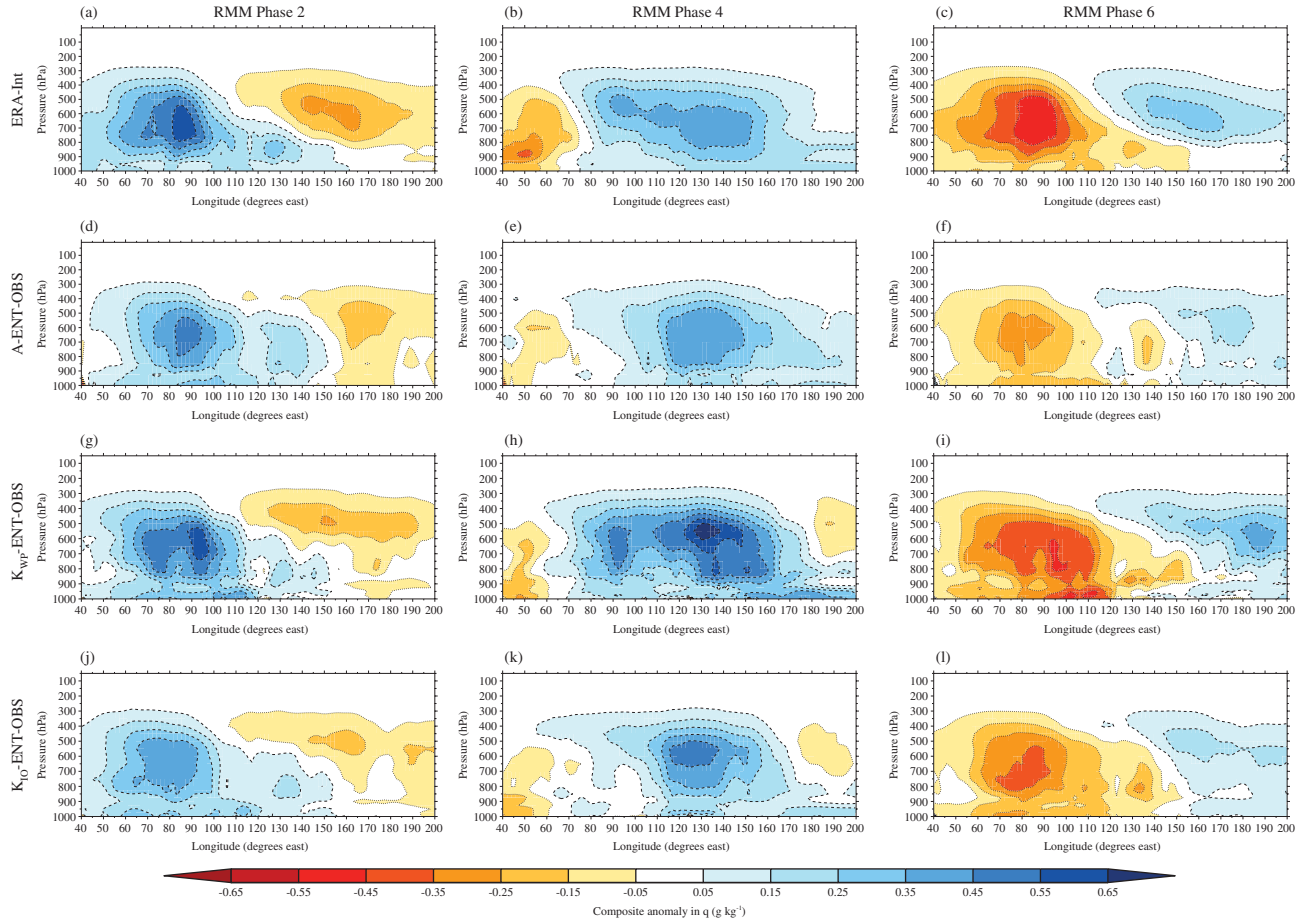

Figure 7. As in Figure 3, but for composites of latitude-averaged (15°S–15°N) anomalies in specific humidity (g kg^{-1}) from (a)–(c) ERA-Interim, (d)–(f) A-ENT, (g)–(i) K_{WP}-ENT-OBS and (j)–(l) K_{IO}-ENT-OBS. Positive (negative) contours are dashed (dotted).

previous active phase, may enhance the suppressed phase and delay the onset of deep convection.

We note that all GA3.0 and GA3.0-KPP integrations show stronger boundary-layer specific-humidity anomalies than ERA-Interim. This is particularly evident in Figure 7(g), for example. This may indicate that convection in GA3.0 is overly sensitive to boundary-layer humidity, rather than free tropospheric humidity. The behaviour does not seem to be caused by increasing F, as A-CTL-OBS and K_{WP}-CTL-OBS (not shown) also display strong boundary-layer anomalies. Further analysis of these features is outside the scope of this study; however, they warrant investigation.

4. Air–sea coupling and MJO propagation

4.1. *The effect of the KPP-coupled mean state*

Section 3.3 suggested that, when GA3.0 has reasonable tropical subseasonal variability, the key effect of coupling is to aid eastward propagation. Despite constraining KPP to climatological SSTs, the mean state of K_{WP}-ENT-OBS differs from A-ENT-OBS, with more precipitation and warmer SSTs in the Maritime Continent (not shown, but similar to Figure 5). To test whether the mean SST changes caused the improved propagation, we prescribe the K_{WP}-ENT-OBS climatological SSTs in A-ENT-K_{WP} (section 2.3). A-ENT-K_{WP} produces a similar distribution of MJO activity in RMM phase space (not shown) to A-ENT-OBS (Figure 1(c)), with an amplitude ≥ 1 on 61.3% of days and relatively lower activity in the Maritime Continent phases. Lag composites of strong events show similar or worse propagation to A-ENT-OBS in all phases (Figure 8(a) and (b)). A-ENT-K_{WP} demonstrates limited eastward propagation in intraseasonal OLR (Figure 9(a)–(c)), particularly from the Indian Ocean through the Maritime Continent. Propagation is more similar to A-ENT-OBS (Figure 4(g)–(i)) than K_{WP}-ENT-OBS (Figure 4(m)–(o)). This experiment confirms that the improved propagation in K_{WP}-ENT-OBS is not due to the effect of coupling on the mean seasonal cycle of tropical SST. The changes in mean precipitation between these experiments are discussed in section 6.

4.2. *Coupling in the Maritime Continent and West Pacific*

Using K_{IO}-ENT-OBS, we examine the sensitivity of the MJO in K_{WP}-ENT-OBS to coupling in the Maritime Continent and the West Pacific by placing the eastern coupling boundary at 100°E (Table 1).

K_{IO}-ENT-OBS has a similar level of MJO activity (61.0%) and distribution in phase space to A-ENT-OBS (Figure 1(c)): the Indian Ocean and West Pacific (Maritime Continent and Western Hemisphere) phases occur relatively more (less) frequently (not shown). Lag composites of strong MJO activity (Figure 8(a) and (b)) show that coupling only in the Indian Ocean reverses the improvements in MJO lifetime and propagation from K_{WP}-ENT-OBS (Figure 2(e)). The composites for strong Indian Ocean (phases 2 and 3) MJO events decay more quickly in K_{IO}-ENT-OBS and fail to extend as far into phase 4 as in K_{WP}-ENT-OBS or observations (Figure 2), indicating that the Maritime Continent is a stronger barrier when coupling only in the Indian Ocean.

The lack of propagation in K_{IO}-ENT-OBS can also be seen in lag regressions of OLR (Figure 9(d)–(f)). Whereas K_{WP}-ENT-OBS showed smooth propagation from the Indian Ocean to the West Pacific (Figure 4(m)), K_{IO}-ENT-OBS displays propagation only to the 100°E coupling boundary (Figure 9(d)). Using a base point at 100°E (Figure 9(e)) shows some propagation from the Indian Ocean, but it is much weaker than in observations and

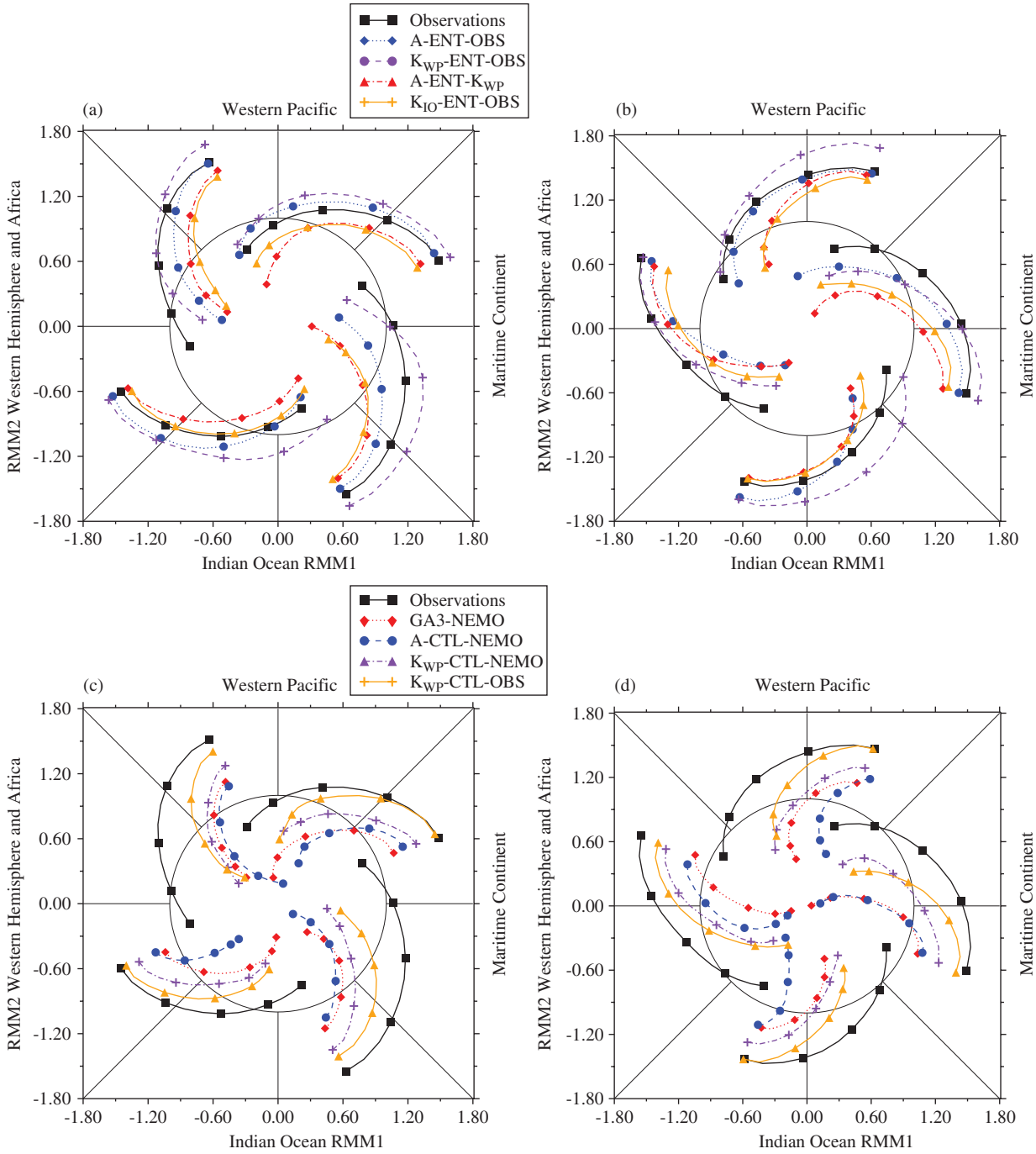

Figure 8. As in Figure 2 but for (a) and (b) A-ENT-OBS (blue), K_{WP}-ENT-OBS (purple), A-ENT-K_{WP} (red) and K_{IO}-ENT-OBS (orange) and for (c) and (d) GA3-NEMO (red), A-CTL-NEMO (blue), K_{WP}-CTL-NEMO (purple) and K_{WP}-CTL-OBS (orange).

K_{WP}-ENT-OBS (Figure 4(b) and (n)) and there is no propagation to the West Pacific.

The structures of moisture anomalies associated with the MJO also degrade in K_{IO}-ENT-OBS. In the phase 2 and phase 4 composites (Figure 7(j) and (k)), positive moisture anomalies terminate sharply near 100°E at most heights. This weakens the westward tilt with height seen in K_{WP}-ENT-OBS (Figure 7(g)–(i)) and ERA-Interim (Figure 7(a)–(c)). There is only a very weak extension of low-level anomalies from the Indian Ocean to the Maritime Continent in K_{IO}-ENT-OBS in phase 2 and of upper-level anomalies from the Maritime Continent to the Indian Ocean in phase 4, compared with K_{WP}-ENT-OBS or reanalysis. The dry anomalies in phase 6 (Figure 7(l)) also decline at the coupling boundary and are weaker than K_{WP}-ENT-OBS and ERA-Interim. In all aspects, the simulated tropical subseasonal variability in K_{IO}-ENT-OBS resembles A-ENT-OBS more strongly than K_{WP}-ENT-OBS.

A-ENT-K_{WP} and K_{IO}-ENT-OBS demonstrate that the key improvement from coupling at 1.5F –propagation through the Maritime Continent –relies upon the realistic simulation of air–sea interactions in the Maritime Continent and West Pacific. Coupling in the Indian Ocean alone is insufficient to produce a realistic MJO in GA3.0.

5. The role of coupled-model mean-state biases

5.1. *Motivation*

In section 3.2, coupling at default F (K_{WP}-CTL-OBS) enhanced the amplitude and propagation of subseasonal tropical convection compared with A-CTL-OBS. The UK Met Office Hadley Centre performed a similar experiment to K_{WP}-CTL-OBS, but with GA3.0 coupled to NEMO (GA3.0-NEMO; section 2.3). Unlike KPP, NEMO includes horizontal ocean dynamics and does

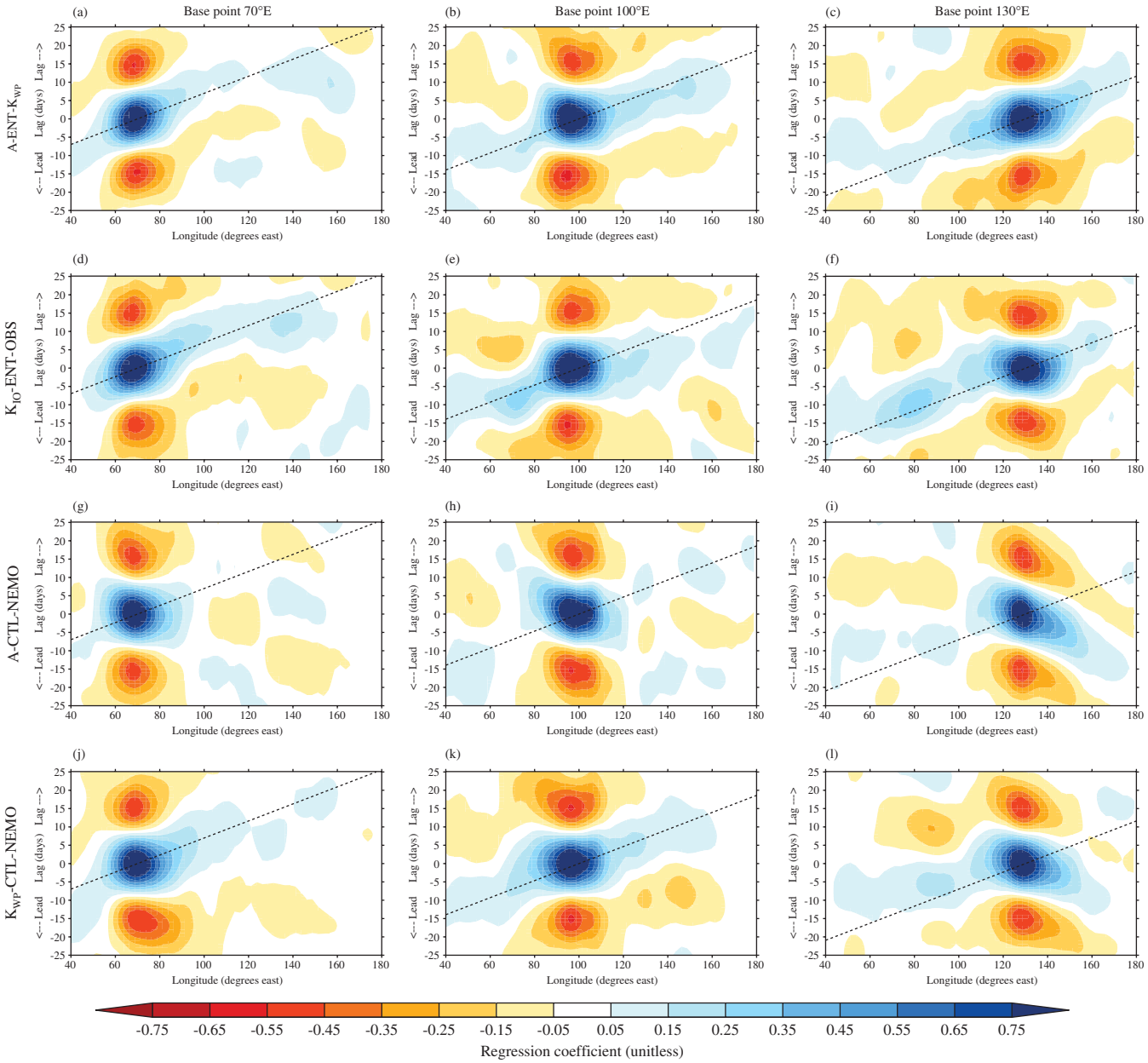

Figure 9. As in Figure 4, but for (a)–(c) A-ENT-K$_{WP}$, (d)–(f) K$_{IO}$-ENT-OBS, (g)–(i) A-CTL-NEMO and (j)–(l) K$_{WP}$-CTL-NEMO.

not use temperature or salinity corrections. Following Bernie *et al.* (2005, 2008), Klingaman *et al.* (2011) and others, and as GA3.0-KPP, GA3.0-NEMO employs a 1 m near-surface ocean vertical resolution and a three-hourly coupling frequency, to improve intraseasonal SST variability. The simulated MJO in GA3.0-NEMO is slightly weaker (36.4% of days with amplitude ≥ 1) than in A-CTL-OBS (40.6%), particularly in the Maritime Continent and Western Hemisphere phases (not shown). There are also no improvements to the propagation or lifetime of composite MJO events (Figure 8(c) and (d)) relative to A-CTL-OBS (Figure 2(a) and (b)). This appears to contradict our result that well-resolved air–sea interactions improve the amplitude and propagation of subseasonal convection in GA3.0 at default *F*.

Coupling to KPP and using climatological heat corrections (section 2.2) results in limited mean SST differences (Figure 5) that do not affect the MJO substantially (section 4.1). GA3.0-NEMO, as with many fully coupled models, produces a considerably different mean state to its atmosphere-only counterpart (A-CTL-OBS; Figure 10). GA3.0-NEMO has colder SSTs throughout the Tropics than the Smith and Murphy (2007) SSTs prescribed in A-CTL-OBS and A-ENT-OBS; the difference approaches 1.5 K in the eastern Indian Ocean and the central equatorial Pacific.

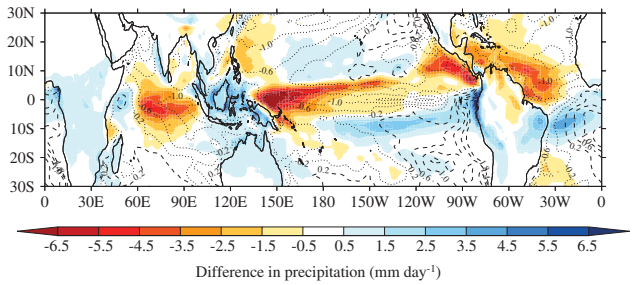

Figure 10. As Figure 5, but for the difference between GA3.0-NEMO and A-CTL-OBS. The difference in SSTs (contour interval 0.4 K, from ±0.2 K) is GA3.0-NEMO minus the Smith and Murphy (2007) ocean analysis.

Consequently, the Indian Ocean and the West Pacific are much drier in GA3.0-NEMO than in A-CTL-OBS.

To understand the extent to which these mean-state differences influence the representation of the MJO in GA3.0-NEMO and hence the diagnosed response of the MJO to coupling, we perform two experiments: A-CTL-NEMO and K$_{WP}$-CTL-NEMO (section 2.3; Table 1). These experiments allow the differences between A-CTL-OBS and GA3.0-NEMO to be decomposed into

(i) the presence of air–sea coupling, absent substantial changes in the mean state (comparing K_{WP}-CTL-NEMO and A-CTL-NEMO), and (ii) the change in the mean state (A-CTL-NEMO versus A-CTL-OBS or K_{WP}-CTL-NEMO versus K_{WP}-CTL-OBS). While (ii) is caused by coupling, it can be thought of as a side effect of simulating air–sea interactions; (i) quantifies the direct impact of air–sea feedback.

5.2. Results

A-CTL-NEMO (33.4%; not shown) has considerably less MJO activity than A-CTL-OBS (40.6%) and somewhat less than GA3.0-NEMO (36.4%), confirming that mean-state biases degrade the MJO in GA3.0-NEMO. MJO activity in A-CTL-NEMO is most severely reduced in the eastern Indian Ocean and Maritime Continent (phases 3 and 4; not shown), the region of coldest SST errors in GA3.0-NEMO (Figure 10(a)). In these phases, the MJO 'decay' probability is 18% (i.e. an MJO event in phase 4 has an 18% chance of decaying into the unit circle on the next day), almost twice that in observations (9.9%, Figure 1(a)), suggesting that MJO events rarely pass from the Indian Ocean to the West Pacific. This is confirmed by RMM lag composites (Figure 8(c) and (d)), which are strongly attracted to the origin in phase space, and by lag regressions of OLR, which show no discernible propagation (Figure 9(g)–(i)).

K_{WP}-CTL-NEMO has improved subseasonal variability over A-CTL-NEMO, even though KPP is constrained to the same mean SSTs as prescribed in A-CTL-NEMO. MJO activity increases by about one third from A-CTL-NEMO (33.4%) to K_{WP}-CTL-NEMO (43.2%), similar to the fractional increase from A-CTL-OBS (40.6%) to K_{WP}-CTL-OBS (55.3%). K_{WP}-CTL-NEMO displays some anticlockwise movement in the RMM lag composites (Figure 8(c) and (d)) and weak eastward propagation of OLR anomalies (Figure 9(j)–(l)). K_{WP}-CTL-NEMO does not simulate a realistic MJO, but by all diagnostics it is an improvement over A-CTL-NEMO. In many phases, K_{WP}-CTL-NEMO is also an improvement over GA3.0-NEMO; the reasons for this are unclear. The MJO in K_{WP}-CTL-NEMO remains weaker than that in K_{WP}-CTL-OBS, however, again demonstrating the degradation from the GA3.0-NEMO mean state. Coupling can improve MJO-like variability even when the mean state strongly suppresses it.

6. Discussion

As in Klingaman and Woolnough (2013), increasing F improves the representation of tropical subseasonal variability in HadGEM3. While that study examined the MJO in a 20-year 1.5F simulation only cursorily, here we have demonstrated that 1.5F primarily increases MJO amplitude, with limited improvements in propagation. The lack of variability in RMM2 in A-ENT-OBS, combined with the decay in RMM amplitude in the lag composites near the Maritime Continent (Figure 2), makes it difficult to reject the hypothesis that subseasonal variability in A-ENT-OBS consists primarily of an anticorrelation between the Indian Ocean and the West Pacific. Such variability would project on to RMM1, but does not resemble the real-world MJO. This emphasizes the need for a range of diagnostics, such as the RMM indices, lag composites and phase composites of several fields, when assessing a model representation of the MJO. Nevertheless, A-ENT-OBS has improved subseasonal variability over A-CTL-OBS.

The comparisons of KPP-coupled and atmosphere-only integrations at default F (A-CTL-OBS and K_{WP}-CTL-OBS) and 1.5F (A-ENT-OBS andK_{WP}-ENT-OBS) strongly suggest that the role of air–sea coupling depends upon the level of subseasonal variability simulated by the AGCM. In K_{WP}-CTL-OBS, as in many previous works (Sperber, 2004; Crueger *et al.*, 2013), adding air–sea interactions to an AGCM with poor intraseasonal variability somewhat improves amplitude and propagation. Even in K_{WP}-CTL-NEMO, when the MJO was strongly suppressed by the GA3.0-NEMO mean state, adding coupling resulted in a modest increase in MJO amplitude and some eastward propagation. Interpreted on their own, as we and others have often done, these results would suggest that coupling is required to bring the level of simulated intraseasonal convection closer to observations.

Yet when the amplitude, if not the spatial distribution, of subseasonal variability in the AGCM approaches observations, as in A-ENT-OBS, coupling has no effect on MJO intensity or frequency (Figure 1). There is nothing to prevent a further increase in MJO activity in K_{WP}-ENT-OBS beyond the observed level or that in A-ENT-OBS; several models have been shown to have 'hyperactive' MJOs (e.g. Hendon, 2000). Rather, K_{WP}-ENT-OBS indicates that when an AGCM is able to simulate strong intraseasonal variability, air–sea coupling no longer provides a positive feedback on that intensity. We obtained these results even when using a 1 m near-surface ocean vertical resolution and sub-daily coupling, generating intraseasonal SST anomalies of comparable magnitude to observations (Figure 6), which past studies showed amplified subseasonal convective activity (Woolnough *et al.*, 2007; Bernie *et al.*, 2008). This supports the hypothesis, presented in section 1.2, that, in AGCMs with poor intraseasonal variability in tropical convection, introducing coupling provides some high-frequency SST anomalies that feed back and amplify what little subseasonal convection exists in the AGCM. It is known that AGCMs respond to prescribed high-frequency SSTs with additional MJO-like activity (Kim *et al.*, 2008; Klingaman *et al.*, 2008a), so it is plausible to construct a similar argument for coupled models. Amplifying those SST anomalies by refining ocean vertical resolution and including the diurnal cycle of air–sea interactions would intensify that effect (Klingaman *et al.*, 2011). It is possible, therefore, that, in AGCMs with poor subseasonal variability, coupling acts as a 'crutch' that amplifies intraseasonal convective anomalies. The mechanism by which this crutch operates requires further studies, the most productive of which may be a systematic set of experiments with several GCMs.

Our K_{WP}-ENT-OBS, A-ENT-K_{WP} and K_{IO}-ENT-OBS experiments indicate that air–sea interactions still have a substantial role in MJO propagation and maintenance, even when the AGCM generates intense, spatially coherent subseasonal convection. The improved MJO propagation in K_{WP}-ENT-OBS over A-ENT-OBS results in a more equitable distribution of activity around phase space, since fewer events decay near the Maritime Continent. A-ENT-K_{WP} demonstrated that this improvement was not due to the relatively small mean SST differences from coupling to KPP. Since we prescribed only the mean seasonal cycle of SST from K_{WP}-ENT-OBS in A-ENT-K_{WP}, it remains possible that the interannual SST variability in K_{WP}-ENT-OBS is somehow responsible for the improved MJO propagation. Further, there are differences in mean precipitation between A-ENT-K_{WP} and K_{WP}-ENT-OBS (not shown), which may be caused by the lack of either interannual SST variability or air–sea coupling in A-ENT-K_{WP}, or some combination of the two. The Maritime Continent (tropical Northwest Pacific) is wetter (drier) in K_{WP}-ENT-OBS by approximately 2 mm day^{-1} in the annual mean; both changes reduce model biases relative to TRMM. Increased moisture in the Maritime Continent may influence MJO propagation in K_{WP}-ENT-OBS. The results of A-ENT-K_{WP} dismiss only the climatological SST differences between K_{WP}-ENT-OBS and A-ENT-OBS.

K_{IO}-ENT-OBS indicates that MJO propagation in GA3.0 requires well-resolved air–sea interactions in the Maritime Continent and West Pacific. This agrees with Weng and Yu (2010), who found that eastward propagation terminated sharply at the coupling boundary when coupling only in the Indian Ocean. Other studies have found coupling in the Indian Ocean to be more important, but many of these have focused on northward propagation during boreal summer (e.g. Lin *et al.*, 2011; Achuthavarier and Krishnamurthy, 2011). One hypothesis

for the influence of coupling on propagation, which is by no means novel, is that air–sea interactions cool SSTs under and to the west of active convection, in the former location from reduced surface fluxes and in the latter from increased wind-driven mixing. At the same time, SSTs east of the convection warm from increased insolation and reduced evaporation. This anomalous SST distribution would stabilize the atmosphere near the enhanced convection while maintaining instability to the east, 'enticing' propagation. SST phase composites from K_{WP}-ENT-OBS support, but cannot confirm, this hypothesis (Figure 6). With no SST anomalies in the Maritime Continent or West Pacific, K_{IO}-ENT-OBS is unable to propagate the MJO out of the Indian Ocean; coupling in the Indian Ocean alone has no effect on either MJO propagation or amplitude in GA3.0.

By coupling with KPP and using climatological heat corrections, we have separated the impacts on the MJO from air–sea interactions as far as possible from those from changes in the tropical mean state. This is an important separation, as mean-state errors may influence not only the level of subseasonal convective variability but also the simulation of air–sea exchanges themselves, for instance by altering mean low-level wind direction (Inness *et al.*, 2003) or air–sea temperature gradients. This framework has allowed us to test the sensitivity of the MJO in the fully coupled model, GA3.0-NEMO, to the mean-state biases in that model. Analyzing only A-CTL-OBS and GA3.0-NEMO would have led us to conclude that air–sea coupling has no effect on, or even worsens, the MJO. K_{WP}-CTL-NEMO and A-CTL-NEMO demonstrate that the direct effect of air–sea interactions is actually to improve the amplitude and propagation of subseasonal convection, albeit modestly and from a very low baseline, but that the GA3.0-NEMO mean state substantially suppresses intraseasonal variability. Many previous sensitivity studies on the role of coupling in the MJO have not separated these effects, or have attempted to do so by prescribing coupled-model SSTs in an AGCM integration. The latter experiment, while somewhat useful, does not consider the the influence of mean-state errors within the coupled framework. These can be assessed here by comparing K_{WP}-CTL-OBS and K_{WP}-CTL-NEMO, which conclusively show that mean-state biases in GA3.0-NEMO weaken an already low level of variability. Further, prescribing SSTs in an AGCM imposes an erroneous lower boundary condition, since AGCMs generally fail to simulate the near-quadrature phase relationship between SSTs and convection (Fu and Wang, 2004). Future experiments exploring the sensitivity of the simulated MJO to air–sea coupling should distinguish the 'direct' impact of coupling –exchanges between the atmosphere and ocean –from the 'indirect' impact –changes to the mean state of the model.

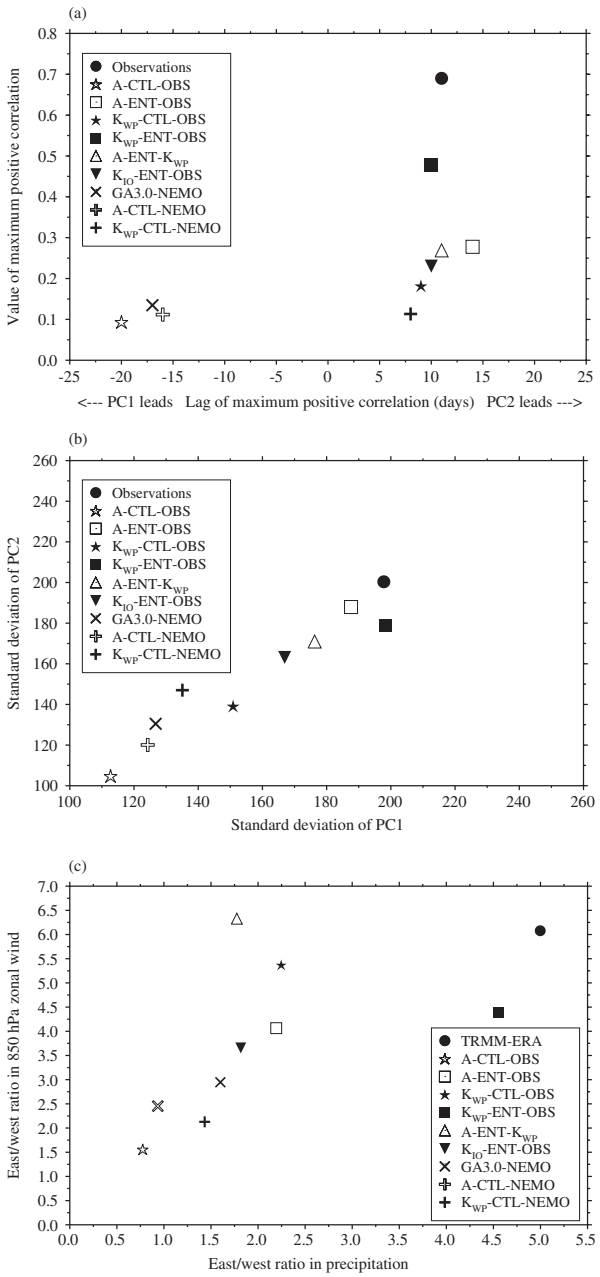

Figure 11. Metrics of the MJO in the simulations performed in this study: the Sperber and Kim (2012) (a) PC1–PC2 lag-correlation metric and (b) the standard deviations of each PC and (c) the east–west power ratio metric described in Kim *et al.* (2009). All unfilled (filled) symbols are GA3.0 (GA3.0-KPP) integrations; corresponding GA3.0 and GA3.0-KPP experiments use the same symbol; all 'closed' symbols (e.g. squares, triangles) are 1.5*F* experiments, while other symbols (e.g. crosses) use default *F*.

7. Summary and conclusions

To summarize the simulated MJO in our experiments, we compute the Sperber and Kim (2012) 'simplified MJO metrics', based on projecting maps of model 20–100 day bandpass-filtered OLR on to the first two EOFs of observed OLR (with the same filtering applied). Lag correlations of the resulting principal component (PC) time series are then computed; the metrics are the maximum positive correlation and the lag at which it occurs (Figure 11(a)). Proximity to observations, which have a correlation of 0.69 at a lag of 11 days, indicates strong eastward propagation with observed phase speed. The standard deviations of the PCs measure MJO amplitude (Figure 11(b)). We also compute the east–west power ratio metric (Kim *et al.*, 2009): the sum of eastward spectral power in wavenumbers 1–3 and periods of 30–80 days divided by the sum of westward power at the same wavenumbers and periods (Figure 11(c)).

We conducted atmosphere-only and coupled experiments to explore the roles of air–sea interactions on the intensity and propagation of the MJO in two configurations of the Hadley Centre model (GA3.0). The configurations differ by a single parameter, *F*, which controls the rates of entrainment and mixing detrainment for diagnosed deep and mid-level convection. Klingaman and Woolnough (2013) found that increasing *F* by 50% (1.5*F*) increased MJO activity in hindcasts and a 20 year simulation. Motivated by those results, we have analyzed how the level of subseasonal convective variability in an atmospheric GCM alters the impact of air–sea interactions on that variability. Initially, we performed four 20 year GA3.0 integrations (Table 1): two atmosphere-only, one at default *F* (A-CTL-OBS) and one with 1.5*F* (A-ENT-OBS); and two coupled to many columns of the KPP boundary-layer ocean in the tropical Indo-Pacific (30°S–30°N, 20°–200°E), as in Klingaman *et al.* (2011), one at default *F* (K_{WP}-CTL-OBS) and one with 1.5*F* (K_{WP}-ENT-OBS). Climatological temperature corrections in KPP maintained similar mean states in coupled and uncoupled experiments (Figure 5), while producing near-observed levels of subseasonal SST variability (Figure 6).

As in Klingaman and Woolnough (2013), A-ENT-OBS (Figure 1(c)) produced a stronger MJO than A-CTL-OBS (Figure 1(b)), bringing GA3.0 closer to observations (Figure 1(a)). Propagation remained deficient in A-ENT-OBS, particularly through the Maritime Continent (Figure 2). A-ENT-OBS produced most of its variability in (Wheeler and Hendon, 2004) RMM1, an anticorrection between the Indian Ocean and the West Pacific, with relatively less in RMM2, which is centred over the Maritime Continent. The lack of consistent propagation led us to conclude that, while A-ENT-OBS was a substantial improvement over A-CTL-OBS, it did not fully capture the MJO. The Sperber and Kim (2012) and east–west power ratio metrics confirm that A-ENT-OBS (unfilled square) has a stronger MJO than A-CTL-OBS (unfilled star) with improved propagation, although propagation remains deficient (Figure 11).

The MJO in K_{WP}-CTL-OBS (Figure 1(d)) was also stronger than A-CTL-OBS, with some eastward propagation (Figure 2), confirming previous studies (Sperber, 2004; Rajendran and Kitoh, 2006) that found that air–sea coupling improved the MJO in AGCMs with deficient subseasonal variability. Amplitude and propagation remained weaker than observed (Figure 11, filled star). At 1.5F, coupling (K_{WP}-ENT-OBS) did not affect overall MJO activity (compare Figure 1(c) and (e)), but considerably improved propagation (Figure 4). This is confirmed by the Sperber and Kim (2012) propagation metric (Figure 11(a), compare unfilled and filled squares) and the east–west power ratio (Figure 11(c)), with little change in the amplitude metric (Figure 11(b)).

The results of an AGCM integration with climatological K_{WP}-ENT-OBS SSTs, A-ENT-K_{WP}, demonstrated that the small mean SST changes from coupling to KPP were not responsible for the improved MJO propagation in K_{WP}-ENT-OBS (section 4.1). Our experiment design cannot dismiss the roles of interannual SST variability or changes in climatological precipitation in MJO propagation, however, so it remains possible that subseasonal air–sea interactions are not the sole cause of the improved MJO in K_{WP}-ENT-OBS (section 6). A sensitivity experiment with coupling only in the Indian Ocean, K_{IO}-ENT-OBS, produced an MJO more similar to A-ENT-OBS than K_{WP}-ENT-OBS (Figure 8(a) and (b)), confirming that air–sea interactions in the Maritime Continent and West Pacific are critical for improved propagation in K_{WP}-ENT-OBS.

The differing impacts of coupling in K_{WP}-CTL-OBS and K_{WP}-ENT-OBS suggest that, for AGCMs with poor tropical subseasonal variability, coupling may provide a 'crutch' that artificially enhances variability in convection via feedback from high-frequency SST anomalies. Since the MJO is primarily an atmospheric mode of variability, A-ENT-OBS provides a better approximation of real-world subseasonal variability than A-CTL-OBS. Based on our experiments, the likely role of coupling in MJO events is to maintain convective anomalies and promote propagation, as in K_{WP}-ENT-OBS, rather than to increase intensity.

A final set of atmosphere-only (A-CTL-NEMO) and KPP-coupled (K_{WP}-CTL-NEMO) integrations demonstrated the ability of the GA3.0-KPP framework to separate cleanly two effects of air–sea interactions in a fully coupled model, GA3.0-NEMO, on simulated subseasonal variability: the inclusion of air–sea exchanges –the 'direct impact' of coupling –and coupled-model mean-state biases –the 'indirect impact'. Comparing GA3.0-NEMO and A-CTL-OBS showed no improvement in MJO activity from coupling, in contrast to comparison of K_{WP}-CTL-OBS and A-CTL-OBS (Figure 11). A-CTL-NEMO and K_{WP}-CTL-NEMO revealed that the small change in activity in GA3.0-NEMO was the result of two larger but offsetting impacts: an increase from the direct impact (comparing K_{WP}-CTL-NEMO and A-CTL-NEMO), but a degradation due to the indirect impact (comparing K_{WP}-CTL-NEMO and K_{WP}-CTL-OBS or A-CTL-NEMO and A-CTL-OBS). If the impacts of coupling are not separated, then changes (or the lack thereof) in intraseasonal variability between AGCM and coupled simulations may be incorrectly attributed to the inclusion of air–sea interactions, when they may be partially or entirely due to mean-state biases.

The mechanisms by which coupling improved the amplitude and propagation of subseasonal convection in K_{WP}-CTL-OBS and the propagation of convection in K_{WP}-ENT-OBS remain unclear. Further experiments, carefully designed to distinguish between the direct and indirect impacts of coupling and using a range of models, are necessary to understand these mechanisms.

Acknowledgements

The authors were funded by the National Centre for Atmospheric Science (NCAS), a collaborative centre of the Natural Environment Research Council. NPK acknowledges productive discussions with Drs Chris Holloway, Stephanie Bush and Linda Hirons. All simulations were performed on HECToR, the UK national high-performance computing service, provided by UoE HPCx Ltd at the University of Edinburgh, Cray Inc. and NAG Ltd, and funded by the Office of Science and Technology through EPSRC's High End Computing Programme.

References

Achuthavarier D, Krishnamurthy V. 2011. Role of Indian and Pacific SST in Indian summer monsoon intraseasonal variability. *J. Clim.* **24**: 2915–2930.

Anderson SP, Weller RA, Lukas RB. 1998. Surface buoyancy forcing and the mixed layer of the Western Pacific warm pool: Observations and 1D model results. *J. Clim.* **9**: 3056–3085.

Arribas A, Glover M, Maidens A, Peterson K, Gordon M, MacLachlan C, Graham R, Fereday D, Camp J, Scaife AA, Xavier P, Colman A, Cusack S. 2011. The GloSea4 ensemble prediction system for seasonal forecasting. *Mon. Weather Rev.* **139**: 1891–1910.

Benedict JJ, Maloney ED. 2013. Tropical intraseasonal variability in version 3 of the GFDL atmosphere model. *J. Clim.* **26**: 426–449.

Bernie DJ, Woolnough SJ, Slingo JM. 2005. Modeling diurnal and intraseasonal variability of the ocean mixed layer. *J. Clim.* **18**: 1190–1202.

Bernie DJ, Guilyardi E, Madec G, Slingo JM, Woolnough SJ, Cole J. 2008. Impact of resolving the diurnal cycle in an ocean–atmosphere GCM. Part 2: A diurnally coupled CGCM. *Clim. Dyn.* **31**: 909–925.

Bhat GS, Gadgil S, Hareesh Kumar PV, Kalsi SR, Madhusoodanan P, Murty VSN, Prasada Rao CVK, Ramesh Babu V, Rao LVG, Rao RR, Ravichandran M, Reddy KG, Sanjeeva Rao P, Sengupta D, Sikka DR, Swain J, Vinayachandran PN. 2001. BOBMEX: The Bay of Bengal monsoon experiment. *Bull. Am. Meteorol. Soc.* **82**: 2217–2243.

Camargo SJ, Wheeler MC, Sobel AH. 2009. Diagnosis of the MJO modulation of tropical cyclogenesis using an empirical index. *J. Atmos. Sci.* **66**: 3061–3074.

Cassou C. 2008. Intraseasonal interaction between the Madden–Julian oscillation and the North Atlantic oscillation. *Nature* **455**: 523–527.

Crueger T, Stevens B, Brokopf R. 2013. The Madden–Julian oscillation in ECHAM6 and the introduction of an objective MJO metric. *J. Clim.* **26**: 3241–3257.

Derbyshire SH, Maidens AV, Milton SF, Stratton RA, Willett MR. 2011. Adaptive detrainment in a convective parameterization. *Q. J. R. Meteorol. Soc.* **137**: 1856–1871.

Fu X, Wang B. 2004. The boreal-summer intraseasonal oscillations simulated in a hybrid coupled atmosphere–ocean model. *Mon. Weather Rev.* **132**: 2628–2649.

Fu X, Wang B, Li T, McCreary JP. 2003. Coupling between northward-propagating, intraseasonal oscillations and sea surface temperature in the Indian Ocean. *J. Atmos. Sci.* **60**: 1733–1753.

Fu X, Wang B, Waliser DE, Tao L. 2007. Impact of atmosphere–ocean coupling on the predictability of monsoon intraseasonal oscillations. *J. Atmos. Sci.* **64**: 157–174.

Goswami BN, Wu G, Yasunari T. 2006. The annual cycle, intraseasonal oscillations, and roadblock to seasonal predictability of the Asian summer monsoon. *J. Clim.* **19**: 5078–5099.

Grabowski WW. 2006. Impact of explicit atmosphere–ocean coupling on MJO-like coherent structures in idealized aquaplanet simulations. *J. Atmos. Sci.* **63**: 2289–2306.

Gregory D, Rowntree PR. 1990. A mass flux convection scheme with representation of cloud ensemble characteristics and stability dependent closure. *Mon. Weather Rev.* **118**: 1483–1506.

Hendon HH. 2000. Impact of air–sea coupling on the Madden–Julian oscillation in a general circulation model. *J. Atmos. Sci.* **57**: 3939–3952.

Hendon HH, Liebmann B. 1990. A composite study of the onset of the Australian summer monsoon. *J. Atmos. Sci.* **47**: 2227–2240.

Hendon HH, Wheeler MC. 2007. Seasonal dependence of the MJO–ENSO relationship. *J. Clim.* **20**: 531–543.

Inness PM, Slingo JM. 2003. Simulation of the Madden–Julian oscillation in a coupled general circulation model. Part I: Comparison with observations and an atmosphere-only GCM. *J. Clim.* **16**: 345–364.

Inness PM, Slingo JM, Guilyardi E, Cole J. 2001. Organization of tropical convection in a GCM with varying vertical resolution: Implications for the simulation of the Madden–Julian Oscillation. *Clim. Dyn.* **17**: 777–793.

Inness PM, Slingo JM, Guilyardi E, Cole J. 2003. Simulation of the Madden–Julian oscillation in a coupled general circulation model. Part II: The role of the basic state. *J. Clim.* **17**: 365–382.

Janicot S, Mounier F, Gervois S, Sultan B, Kiladis G. 2010. Dynamics of the West African monsoon. Part V: The detection and role of the dominant modes of convectively coupled equatorial Rossby waves. *J. Clim.* **23**: 4005–4024.

Jia X, Li C, Ling J, Zhang C. 2008. Impacts of a GCM's resolution on MJO simulation. *Adv. Atmos. Sci.* **25**: 139–156.

Jones C, Waliser DE, Gautier C. 1998. The influence of the Madden–Julian oscillation on ocean surface heat fluxes and sea surface temperature. *J. Clim.* **11**: 1057–1072.

Kemball-Cook S, Wang B, Fu X. 2002. Simulation of the ISO in the ECHAM4 model: The impact of coupling with an ocean model. *J. Atmos. Sci.* **59**: 1433–1453.

Kessler WS, McPhaden MJ, Weickmann KM. 1995. Forcing of intra-seasonal Kelvin waves in the equatorial Pacific. *J. Geophys. Res.* **100**: 10613–10613.

Khairoutdinov M, Randall D, DeMott C. 2005. Simulation of the atmospheric general circulation using a cloud-resolving model as a superparameterisation of physical processes. *J. Atmos. Sci.* **62**: 2136–2154.

Kim HM, Hoyos CD, Webster PJ, Kang IS. 2008. Sensitivity of MJO simulation and predictability to sea surface temperature variability. *J. Clim.* **21**: 5304–5317.

Kim D, Sperber K, Stern W, Waliser D, Kang IS, Maloney E, Wang W, Weickmann K, Benedict J, Khairoutdinov M, Lee MI, Neale R, Suarez M, Thayer-Calder K, Zhang G. 2009. Application of MJO simulation diagnostics to climate models. *J. Clim.* **22**: 6413–6436.

Kim HM, Hoyos CD, Webster PJ, Kang IS. 2010. Ocean–atmosphere coupling and the boreal winter MJO. *Clim. Dyn.* **35**: 771–784, doi: 10.1007/s00 382-009-612-x.

Klingaman NP, Woolnough SJ. 2013. Using a case-study approach to improve the Madden–Julian oscillation in the Hadley Centre model. *Q. J. R. Meteorol. Soc.*, doi:10.1002/qj.2314.

Klingaman NP, Inness PM, Weller H, Slingo JM. 2008a. The importance of high-frequency sea-surface temperature variability to the intraseasonal oscillation of Indian monsoon rainfall. *J. Clim.* **21**: 6119–6140.

Klingaman NP, Weller H, Slingo JM, Inness PM. 2008b. The intraseasonal variability of the Indian summer monsoon using TMI sea-surface temperatures and ECMWF reanalysis. *J. Clim.* **21**: 2519–2539.

Klingaman NP, Woolnough SJ, Weller H, Slingo JM. 2011. The impact of finer-resolution air–sea coupling on the intraseasonal oscillation of the Indian summer monsoon. *J. Clim.* **24**: 2451–2468.

Kummerow C, Barnes W, Kozu T, Shiue J, Simpson J. 1998. The Tropical Rainfall Measuring Mission (TRMM) sensor package. *J. Atmos. Oceanic Technol.* **15**: 809–817.

Large W, McWilliams J, Doney S. 1994. Oceanic vertical mixing: A review and a model with a nonlocal boundary layer parameterization. *Rev. Geophys.* **32**: 363–403.

Lavender SL, Matthews AJ. 2009. Respose of the West African monsoon to the Madden–Julian oscillation. *J. Clim.* **22**: 4097–4116.

Liess S, Bengtsson S. 2004. The intraseasonal oscillation in ECHAM4 Part II: Sensitivity studies. *Clim. Dyn.* **22**: 671–688.

Liess S, Bengtsson L, Arpe K. 2004. The intraseasonal oscillation in ECHAM4. Part I: Coupled to a comprehensive ocean model. *Clim. Dyn.* **22**: 671–688.

Lin JL, Kiladis GN, Mapes BE, Weickmann KM, Sperber KR, Lin W, Wheeler M, Shubert SD, Del Genio A, Donner LJ, Emori S, Gueremy JF, Hourdain F, Rasch PJ, Roeckner E, Scinocca JF. 2006. Tropical intraseasonal variability in 14 IPCC AR4 climate models. Part I: Convective signals. *J. Clim.* **19**: 2665–2690.

Lin A, Li T, Fu X, Luo JJ, Masumoto Y. 2011. Effects of air–sea coupling on the boreal summer intraseasonl oscillations over the tropical Indian Ocean. *Clim. Dyn.* **37**: 2303–2322.

Madden RA, Julian PR. 1971. Detection of a 40–50 day oscillation in the zonal wind in the tropical Pacific. *J. Atmos. Sci.* **28**: 702–708.

Newman M, Sardeshmukh PD, Penland C. 2009. How important is air–sea coupling in ENSO and MJO evolution. *J. Clim.* **22**: 2958–2977.

Pai DS, Bhate J, Sreejith OP, Hatwar HR. 2011. Impact of MJO on the intraseasonal variation of summer monsoon rainfall over India. *Clim. Dyn.* **36**: 41–55.

Rajendran K, Kitoh A. 2006. Modulation of tropical intraseasonal oscillations by atmosphere–ocean coupling. *J. Clim.* **19**: 366–391.

Reicher T, Roads JO. 2005. Long-range predictability in the Tropics, Part II: 30–60-day variability. *J. Clim.* **18**: 634–650.

Slingo JM, Sperber KR, Boyle JS, Ceron JP, Dix M, Dugas B, Ebisuzaki W, Fyfe J, Gregory D, Gueremy JF, Hack J, Harzallah A, Inness P, Kitoh A, Lau WKM, McAvaney B, Madden R, Matthews A, Palmer TN, Park CK, Randall D, Renno N. 1996. Intraseasonal oscillations in 15 atmospheric general circulation models: Results from an AMIP diagnostic subproject. *Clim. Dyn.* **12**: 325–357.

Smith DM, Murphy JM. 2007. An objective ocean temperature and salinity analysis using covariances from a global climate model. *J. Geophys. Res.* **112**: C02022.

Sperber KR. 2004. Madden–Julian variability in NCAR CAM2.0 and CCSM2.0. *Clim. Dyn.* **23**: 259–278.

Sperber KR, Annamalai H. 2008. Coupled model simulations of boreal summer intraseasonal (30–50 day) variability. Part 1: Systematic errors and caution on use of metrics. *Clim. Dyn.* **31**: 345–372.

Sperber KR, Kim D. 2012. Simplified metrics for the identification of the Madden–Julian oscillation in models. *Atmos. Sci. Lett.* **13**: 187–193.

Sperber KR, Gualdi S, Legutke S, Gayler V. 2005. The Madden–Julian oscillation in ECHAM4 coupled and uncoupled general circulation models. *Clim. Dyn.* **25**: 117–140.

Stratton RA, Stirling A, Derbyshire S. 2009. *'Changes and developments to convective momentum transport (CMT) parameterization based on analysis of CRM and SCM'*, Technical Report 590. Forecasting R&D, Met Office: Exeter, UK.

Uppala SM, Kållberg PW, Simmons AJ, Andrae U, da Costa Bechtold V, Fiorino M, Gibson JK, Haseler J, Hernandez A, Kelly GA, Li X, Onogi K, Saarinen S, Sokka N, Allan RP, Andersson E, Arpe K, Balmaseda MA, Beljaars ACM, van de Berg L, Bidlot J, Bormann N, Caires S, Chevallier F, Dethof A, Dragosavac M, Fisher M, Fuentes M, Hagemann S, Hólm E, Hoskins BJ, Isaksen L, Janssen PAEM, Jenne R, McNally AP, Mahfouf JF, Morcrette JJ, Rayner NA, Saunders RW, Simon P, Sterl A, Trenberth KE, Untch A, Vasiljevic D, Viterbo P, Woolen J. 2005. The ERA-40 re-analysis. *Q. J. R. Meteorol. Soc.* **131**: 2961–3012.

Valcke S, Caubel A, Declat D, Terray L. 2003. *'OASIS3 Ocean Atmosphere Sea Ice Soil user's guide'*, Technical Report TR/CMGC/03/69. CERFACS: Toulouse, France.

Vecchi GA, Harrison DE. 2002. Monsoon breaks and subseasonal sea surface temperature variability in the Bay of Bengal. *J. Clim.* **15**: 1485–1493.

Vitart F. 2009. Impact of the Madden Julian oscillation on tropical storms and risk of landfall in the ECMWF forecast system. *Geophys. Res. Lett.* **36**: L15802.

Vitart F, Molteni F. 2010. Simulation of the Madden–Julian oscillation and its teleconnections in the ECMWF forecast system. *Q. J. R. Meteorol. Soc.* **136**: 842–855.

Waliser D, Murtugudde R, Lucas LE. 2004. Indo-Pacific Ocean response to atmospheric intraseasonal variability: 2. Boreal summer and the intraseasonal oscillation. *J. Geophys. Res.* **109**: C03030.

Walters DN, Best MJ, Bushell AC, Copsey D, Edwards JM, Falloon PD, Harris CM, Lock AP, Manners JC, Morcrette CJ, Roberts MJ, Stratton RA, Webster S, Wilkinson JM, Willett MR, Boutle IA, Earnshaw PD, Hill PG, MacLachlan C, Martin GM, Moufouma-Okia W, Palmer MD, Petch JC, Rooney GG, Scaife AA, Williams KD. 2011. The Met Office Unified Model Global Atmosphere 3.0/3.1 and JULES Global Land 3.0/3.1 configurations. *Geosci. Model Dev.* **4**: 919–941.

Weng SP, Yu JY. 2010. Impacts of Pacific and Indian Ocean coupling on wintertime tropical intraseasonal oscillatioon: a basin-coupling CGCM study. *Int. J. Climatol.* **30**: 359–371.

Wentz FJ. 2000. Satellite measurements of sea surface temperature through clouds. *Science* **288**: 847–850.

Wheeler MC, Hendon HH. 2004. An all-season real-time multivariate MJO index: Development of an index for monitoring and prediction. *Mon. Weather Rev.* **132**: 1917–1932.

Wheeler MC, Hendon HH, Cleland S, Meinke H, Donald A. 2009. Impacts of the Madden–Julian oscillation on Australian rainfall and circulation. *J. Clim.* **22**: 1482–1498.

Woolnough SJ, Slingo JM, Hoskins BJ. 2000. The relationship between convection and sea surface temperatures on intraseasonal timescales. *J. Clim.* **13**: 2086–2104.

Woolnough SJ, Slingo JM, Hoskins BJ. 2001. The organization of tropical convection by intraseasonal sea surface temperature anomalies. *Q. J. R. Meteorol. Soc.* **127**: 887–907.

Woolnough SJ, Vitart F, Balmaseda MA. 2007. The role of the ocean in the Madden–Julian Oscillation: Implications for MJO prediction. *Q. J. R. Meteorol. Soc.* **133**: 117–128.

Yang GY, Slingo J, Hoskins B. 2009. Convectively coupled equatorial waves in high-resolution Hadley Centre climate models. *J. Clim.* **22**: 1897–1919.

Zhu H, Hendon HH, Jakob C. 2009. Convection in a parameterized and superparameterized model and its role in the representation of the MJO. *J. Atmos. Sci.* **66**: 2796–2811.